Resonance fluorescence of single Barium ions

Diplomarbeit

zur Erlangung des Magistergrades an der
naturwissenschaftlichen Fakultät
der Leopold-Franzens-Universität Innsbruck

vorgelegt von

Hilmar Oberst

durchgeführt am Institut für Experimentalphysik
unter der Leitung von
o. Univ. Prof. Dr. R. Blatt

Innsbruck
April 1999

Contents

Contents

1 Introduction

Newton considered light to be a jet of particles, which for example rebound when striking a mirror. In the course of the first half of the 19$^{\text{th}}$ century the wave-like nature of light was proved by diffraction experiments. Optics was integrated into electromagnetic theory, the velocity of light could be related to electric and magnetic constants and polarization phenomena were interpreted as a manifestation of the vector character of the electric field. However, in 1900 Planck discovered that the spectrum of the black-body radiation could be explained by assuming the quantization of energy: The energy of an electro-magnetic wave of frequency ν is restricted to multiples of the quantum $h\nu$. Although this hypothesis allowed to explain the photoelectric effect it was not until 1924 that the effect of single photons could be demonstrated by the Compton effect.

Today the properties of light are described within the framework of modern quantum theory. It has become possible to generate "non-classical light", i.e. light whose properties cannot be described by classical electrodynamics. In this regard photon counting experiments such as the Hanbury-Brown-Twiss experiment [1, 2], which was first performed in 1956, played an important role. A beam splitter and two photomultipliers are used to record the coincidences of photo electric events. For a thermal light source the measured photon correlation shows the effect of bunching: The probability of detecting two photons within a time delay τ has its maximum around $\tau = 0$, i.e. the light quanta arrive preferably in "bunches". The reverse effect that the photon correlation has its minimum at $\tau = 0$, called anti-bunching [3, 4], was measured for the first time in the resonance fluorescence from an atomic beam in 1977 [5, 6]. Anti-bunching is a pure quantum phenomenon, reflecting the preparation of the atom in its ground state after emission of a photon. Other pure quantum effects are the observation of squeezed light [7–9] or the preparation of entangled photon states [10].

The properties of light must necessarily be studied in connection with the light sources. In fact another main stream in the early formulation of quantum theory was concerned with the explanation of spectral lines of atoms. Bohr's model of the atom was the first approach to a quantum mechanical description of atoms. The discrete energy levels were characterized by only one quantum number, spectral lines resulting from transitions of the atom from a state of higher energy to a state of lower energy by

emission of a photon. Although Bohr's model was replaced by a full quantum theory, the analysis of spectral lines, i.e. spectroscopy, remained the main source of information about atomic energy levels.

Development of quantum mechanics as well as the more and more improved spectroscopic resolution led to a deep understanding of the atomic structure and the related spectra. A splitting of spectral lines was found, the fine structure, which could be explained with the coupling of the electron spin to the orbital momentum together with the relativistic behavior of the electron. The magnetic moment of the atomic nucleus accounts for the hyperfine splitting. The interaction of the atom with the surrounding radiation field leads to additional shifts of the energy levels (Lamb-shift [11, 12]) and to spontaneous decay of all excited states [13].

The progress in spectroscopy, as well as the development of quantum optics, are unthinkable without the invention of lasers in the early 1960s. Their narrow emission bandwidth, which can be reduced far below the width of spectral lines, and their high light intensities are the base for laser spectroscopy and non-linear optics. Today diode lasers are used in many applications: The spectral ranges in which they are available have been expanding, now reaching the ultra-violet region. With the help of optical feedback and electronic stabilization their laser linewidth can be much reduced. A reduction to less than 1 kHz has been achieved [14].

In laser spectroscopy an atomic sample is illuminated with an external laser light source. The spectral resolution as well as the properties of the emitted fluorescent light depend on the preparation of the investigated atoms. In a gas cell, for example, the motion of the atoms leads to Doppler and collision broadening of the spectral lines. The spectral resolution is also reduced when the interaction time with the laser beam is limited by the time of flight of the atoms. Various techniques have been developed to overcome these limitations, such as saturation and two-photon spectroscopy, which are Doppler free techniques, and Ramsey spectroscopy, which reduces the broadening due to a limited interaction time [15].

The ideal case for precision spectroscopy is the preparation of a single, motionless particle. This can be achieved by the trapping of ions with electric fields in a Paul trap, which was first proposed in 1975 [16, 17]. This technique has several advantages: First there is no restriction on the interaction time. Ions can be stored for an almost unlimited period. Secondly the ion motion can be damped with the help of laser cooling. The energy of the ion can be reduced so far that the oscillation amplitude of the ion in the trap is smaller than the light wavelength. Then the first order Doppler effect is nearly completely suppressed. Eventually, it is possible to confine only one single particle, which was first demonstrated in 1980 [18]. Under UHV conditions the measurement then is not disturbed by collisions with other particles. The properties of a single ion can be studied through its resonance fluorescence.

This thesis is part of an ongoing experimental project, which aims at measuring the

non-classical properties and the spectrum of resonance fluorescence from a single Ba^+ ion. The ion is confined in a Paul trap and illuminated with two coherent laser light fields. The properties of the detected fluorescent light reveal the internal dynamics, i.e. the population and coherences of the atomic energy levels, and the external dynamics of the ion, i.e. its motion in the trap. In the course of this thesis the quantum mechanical model describing the interaction between the light fields and the Ba^+ ion, and the influence of the oscillation in the trap was implemented in computer programs. The fit of the numerically calculated curves to the measured data provides one of the basic tools for determining the experimental parameters, which are needed to characterize the system and predict its behavior in further measurements or applications.

Several types of measurements were performed. One type of measurement was the registration of excitation spectra, i.e. the intensity of the fluorescent light versus the detuning of either of the lasers. For this purpose it was necessary to improve the setup of one of the lasers: An acousto-optical modulator was inserted that allowed to exactly detune the laser frequency.

The thesis is organized as follows:

Chapter 2 and 3 introduce the theory of the interaction between the Ba^+ ion and the two light fields. The formalism is adapted to the particular experimental setup and the implementation of the model in computer programs. The aim is to show the way from the general quantum mechanical description of the light-matter interaction to the particular form of the equations used in the programs. The trapping of an ion in a Paul trap and the influence of its motion on the resonance fluorescence are discussed in chapter 4. The experimental setup is described in chapter 5. In chapter 6 the results of the different measurements are presented.

2 The interaction of a three level system with two coherent light fields

2.1 Introduction

The aim of the experiment discussed in this thesis is to analyse the interaction of single Barium ions stored in a radio frequency trap with two near resonant laser light fields. We are particularly interested in the physical properties of the light scattered by the ion, that is the intensity, the photon counting distribution and the spectrum of the single ion resonance fluorescence.

This chapter gives a first introduction to the quantum mechanical description of the ion, the laser light fields and their interaction. In our experiment singly ionized ^{138}Ba-atoms are used. Their electron configuration corresponds to that of the noble gas Xenon with one additional valence electron ([Xe]6^2S$_{1/2}$).

Transition	λ_{air} (nm)	Γ_{nat} (MHz)
6^2S$_{1/2}$ $\Leftrightarrow$ 6^2P$_{1/2}$	493.4	15.1
6^2P$_{1/2}$ $\Leftrightarrow$ 5^2D$_{3/2}$	649.7	5.3
6^2P$_{3/2}$ $\Leftrightarrow$ 6^2S$_{1/2}$	455.4	18.8
6^2P$_{3/2}$ $\Leftrightarrow$ 5^2D$_{5/2}$	614.2	5.9
6^2P$_{3/2}$ $\Leftrightarrow$ 5^2D$_{3/2}$	585.4	0.7
5^2D$_{3/2}$ $\Leftrightarrow$ 6^2S$_{1/2}$	2051	0.4 $\cdot 10^{-8}$
6^2S$_{1/2}$ $\Leftrightarrow$ 5^2D$_{5/2}$	1761.7	0.5 $\cdot 10^{-8}$

Table 2.1: Wavelengths and decay rates of the ^{138}Ba$^+$ fine structure transitions [19].

Figure 2.1 shows the relevant part of the fine-structure level scheme of ^{138}Ba$^+$ and table 2.1 summarizies the corresponding wavelengths and decay rates. In Barium ions, as well as in Calcium, Strontium and Mercury ions, two D levels lie between the S and the P levels [20]. (The Mercury ion has the additional oddity that the $D_{5/2}$ and $D_{3/2}$ levels are inverted). The S $\Leftrightarrow$ P and the D $\Leftrightarrow$ P transitions are dipole-allowed and the corresponding decay rates are in the order of $10^6\ s^{-1}$. The D-levels have lifetimes
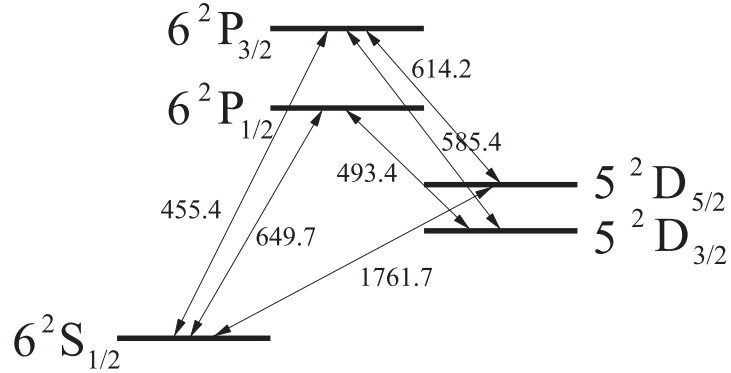
Figure 2.1: Fine structure level scheme of ^{138}Ba$^+$. All wavelengths are given in nm.

of 30s and 40s, respectively, and decay into the S-level happens only via an electric quadrupole transition.

Since the nucleus of ^{138}Ba$^+$ has no spin (I=0), there is no hyperfine splitting of the atomic energy levels. However, the energy levels split up into several Zeeman-components in an external magnetic field. In order to obtain a correct description of the Barium ion it is necessary to take all the Zeeman sublevels into consideration, which will be done in detail in chapter 3. For the moment, however, we concentrate on the simpler case where the ion is assumed to have only three relevant energy levels that are coupled by two coherent light fields.

The wavelengths of the two lasers used to illuminate the ion are at 493 nm and 650 nm, corresponding to the 6^2S$_{1/2} \Leftrightarrow 6^2P_{1/2}$ and 6^2P$_{1/2} \Leftrightarrow 5^2D_{3/2}$ transitions. All other energy levels are far off resonance. They can neither be excited by the lasers nor be populated via spontaneous decay. Hence we have a closed system with three relevant energy levels.

The laser at 493 nm shines in a green and the laser at 650 nm in a red color. Therefore all quantities related to the S $\Leftrightarrow$ P transition are indexed with 'g' whereas the index 'r' is attached to quantities corresponding to the P $\Leftrightarrow$ D transition.

The light emitted by an atom which is excited with resonant light fields is called resonance fluorescence. In our experiment the fluorescent photons are observed in a direction perpendicular to the laser beam direction. It should be noted that these photons are due exclusively to spontaneous emission. When the emission is stimulated then the emitted photons are in the same light mode as the photons that induced the transition.

If $\rho_{22}(t)$ describes the probability of finding the ion in the excited state ($6^2\mathrm{P}_{1/2}$) at time t, then the average numbers of green and red fluorescence photons, $\langle n \rangle_g$ and $\langle n \rangle_r$, counted by a photo multiplier perpendicular to the laser beam direction in the time interval T are

$$\langle n \rangle_g(T) = \eta_g \int_t^{t+T} \rho_{22}(\tau)\Gamma_g \, d\tau \tag{2.1}$$

$$\langle n \rangle_r(T) = \eta_r \int_t^{t+T} \rho_{22}(\tau)\Gamma_r \, d\tau \tag{2.2}$$

where Γ_g and Γ_r are the decay rates on the S $\Leftrightarrow$ P and P $\Leftrightarrow$ D transitions. η_g and η_r denote the detection efficiencies: They depend on the imaging optics and on the quantum efficiencies of the photomultiplier. If the atom is in a steady state, i.e. when T is sufficiently large, then it is easily seen that the photon counting rates are

$$\frac{\langle n \rangle_{g,r}(T)}{T} \propto \rho_{22}(\infty). \tag{2.3}$$

2.2 Description of the atom, the light fields and the dipole interaction

The Hamiltonian of the system is constituted of three parts: The Hamiltonian of the atom, of the light field and the one describing the interaction.

$$\hat{\mathcal{H}} = \hat{\mathcal{H}}_{atom} + \hat{\mathcal{H}}_{field} + \hat{\mathcal{H}}_{int} \tag{2.4}$$

Let $|a\rangle$, $a = 1, 2, 3$, denote the eigenvectors of the atomic Hamiltonian. The $6^2S_{1/2}$ state corresponds to $|1\rangle$, $6^2P_{1/2}$ to $|2\rangle$ and $5^2D_{3/2}$ to $|3\rangle$.

$$\hat{\mathcal{H}}_{atom}|a\rangle = \hbar\omega_a|a\rangle \tag{2.5}$$

ω_a are the atomic Bohr frequencies. Then $\hat{\mathcal{H}}_{atom}$ can be written as

$$\hat{\mathcal{H}}_{atom} = \sum_{a=1}^{3} \hbar\omega_a|a\rangle\langle a|. \tag{2.6}$$

The Hamiltonian of a light mode, characterized by frequency ω_k, wavevector $\vec{k}$ and polarization $\vec{\epsilon_k}$, has the same form as the quantum-mechanical Hamiltonian of a one dimensional harmonic oscillator.

$$\hat{\mathcal{H}}_k = \hbar\omega_k(\hat{a}_k^\dagger\hat{a}_k + 1/2) \tag{2.7}$$

where $\hat{a}_k^\dagger$ and $\hat{a}_k$ are the photon destruction and creation operators.

The eigenvectors of this Hamiltonian are usually called the number states $|n\rangle$, $n = 0, 1, 2, \ldots$ since they represent a quantum-mechanical state of the light field, which contains n photons, each with energy $\hbar\omega_k$. The action of $\hat{\mathcal{H}}$, $\hat{a}$ and $\hat{a}^\dagger$ on the number states is defined by

$$\hat{\mathcal{H}}|n\rangle = \hbar\omega(n + 1/2)\,|n\rangle \tag{2.8}$$

$$\hat{a}|n\rangle = \sqrt{n}\,|n - 1\rangle \tag{2.9}$$

$$\hat{a}^\dagger|n\rangle = \sqrt{n + 1}\,|n + 1\rangle. \tag{2.10}$$

The light fields of real light sources do not have definite numbers of photons, however, but are either statistical mixtures, as in the case of thermal excitation, or linear superpositions, as in the case of the coherent photon states, of the number states. The coherent states are defined as the following superpositions:

$$|\alpha\rangle \;=\; \exp(-\frac{1}{2}|\alpha|^2) \sum_{n=0}^{\infty} \frac{\alpha^n}{(n!)^{1/2}}|n\rangle \tag{2.11}$$

$$\alpha \;=\; |\alpha|e^{i\theta} \in \mathbb{C} \tag{2.12}$$

They are the closest quantum mechanical approximation to a classical monochromatic electromagnetic wave [21]. A single mode laser generates a coherent state, which is therefore chosen to describe the two laser light fields in our experiment. It is readily shown that

$$\langle\alpha|\alpha\rangle \;=\; 1 \tag{2.13}$$

$$\hat{a}|\alpha\rangle \;=\; \alpha\,|\alpha\rangle \tag{2.14}$$

$$\langle a|\hat{a}^\dagger \;=\; \alpha^*\,\langle\alpha| \tag{2.15}$$

and hence

$$\langle\alpha|\hat{a}^\dagger\hat{a}|\alpha\rangle = |\alpha|^2. \tag{2.16}$$

The single mode quantum mechanical field operator is [21]

$$\hat{\vec{E}}(\vec{r}, t) = i\vec{\epsilon}\left(\frac{\hbar\omega}{2\epsilon_0 V}\right)^{1/2} \{\hat{a}\exp(-i\omega t + i\vec{k}\cdot\vec{r}) - \hat{a}^\dagger\exp(+i\omega t - i\vec{k}\cdot\vec{r})\} \tag{2.17}$$

where V denotes the quantization volume and $\vec{\epsilon}$ is a unit vector indicating the polarization direction.

By evaluating the expectation value of the electric field operator for the coherent photon state $|\alpha\rangle$, we obtain

$$\langle\alpha|\hat{\vec{E}}|\alpha\rangle = -2\vec{\epsilon}\left(\frac{\hbar\omega}{2\epsilon_0 V}\right)^{1/2}|\alpha|\sin(\vec{k}\cdot\vec{r}-\omega t+\theta) \tag{2.18}$$

which corresponds to a classical wave, whose electric field amplitude is related to $|\alpha|$ by

$$E_0 := 2\left(\frac{\hbar\omega}{2\epsilon_0 V}\right)^{1/2}|\alpha|. \tag{2.19}$$

In our case the Hamiltonian of the field is

$$\hat{\mathcal{H}}_{field} = \hbar\omega_g(\hat{a}_g^\dagger\hat{a}_g + 1/2) + \hbar\omega_r(\hat{a}_r^\dagger\hat{a}_r + 1/2) \tag{2.20}$$

and the electric field operator

$$\hat{\vec{E}} = \hat{\vec{E}}_g + \hat{\vec{E}}_r \tag{2.21}$$

with $\hat{\vec{E}}_g$ and $\hat{\vec{E}}_r$ defined analogously to equation (2.17). The spatial dependence $\vec{k}\cdot\vec{r}$ over the extension of the ion is on the order of $\frac{a_{Bohr}}{\lambda}\approx 10^{-4}$ and can be neglected.

A general state of the system can finally be written as

$$|\Psi\rangle = |a\rangle\otimes|\alpha_g\rangle\otimes|\alpha_r\rangle = |a\,\alpha_g\,\alpha_r\rangle. \tag{2.22}$$

If the frequencies of the lasers are close to the atomic transition frequencies, then the ion may be excited to the P state by absorption of a photon or may decay to one of the ground states by emission of a photon. These processes can be described with an interaction Hamiltonian of the following form:

$$\hat{H}_{int} = -\hat{\vec{D}}\cdot\hat{\vec{E}} \tag{2.23}$$

where $\hat{\vec{D}}$ represents the atomic dipole operator. It is assumed here, that the light field interacts only with the electric dipole-moment and not with electric or magnetic moments of higher order. Since the S-D transition is dipole-forbidden, the D level is treated as a stable energy level in this model. In view of the long life-times of the D-levels (table 2.1) this is of course a good approximation for processes that happen on a sub-second time scale.

The atomic dipole operator

$$\vec{D} = e\begin{pmatrix} x \\ y \\ z \end{pmatrix} \tag{2.24}$$

can also be expressed with the help of the atomic eigenvectors

$$\vec{D} \;=\; \sum_{a,b=1,2,3} \vec{D}_{ab}|a\rangle\langle b| \tag{2.25}$$

$$\vec{D}_{ab} \;=\; \langle a|\vec{D}|b\rangle. \tag{2.26}$$

By considering the odd parity of x,y,z and by assuming that $\vec{D}_{ab}$ are real numbers, we obtain

$$\vec{D} = \vec{D}_{12}(|1\rangle\langle 2| + |2\rangle\langle 1|) + \vec{D}_{23}(|2\rangle\langle 3| + |3\rangle\langle 2|). \tag{2.27}$$

The operator $|a\rangle\langle b|$, applied to an atomic state, shifts the electron from state $|b\rangle$ to state $|a\rangle$. The interaction Hamiltonian

$$\hat{\mathcal{H}}_{int} = -\left(\vec{D}_{12}(|1\rangle\langle 2| + |2\rangle\langle 1|) + \vec{D}_{23}(|2\rangle\langle 3| + |3\rangle\langle 2|)\right)\left(\hat{\vec{E}}_g + \hat{\vec{E}}_r\right) \tag{2.28}$$

involves products of the photon destruction and creation operators with the atomic transition operators $|a\rangle\langle b|$. The terms can easily be interpreted as simple optical processes:

$\hat{a}_g\,|2\rangle\langle 1|$ represents the destruction of a photon of the green laser light field and a transition from the S to the P level.

$|1\rangle\langle 2|\,\hat{a}_g^{\dagger}$ is the reverse process: creation of a photon by transition from the P to the S level.

The events represented by $\hat{a}_g^{\dagger}\,|2\rangle\langle 1|$ or $\hat{a}_g\,|1\rangle\langle 2|$, where a photon is created and the atom is excited at the same time or vice versa, do not conserve energy. They are allowed only in higher order optical processes, in which energy conservation may be violated in intermediate steps. These weak higher order contributions are neglected, which is equivalent to what is usually called "rotating-wave approximation" in semi-classical models. Using similar arguments it is also assumed that the green laser interacts only with the S $\leftrightarrow$ P and the red laser with the P $\leftrightarrow$ D transition, i.e. terms such as $\hat{a}_r|2\rangle\langle 1|$ and $\hat{a}_g|3\rangle\langle 1|$ are omitted.

We finally obtain the interaction Hamiltonian:

$$\hat{\mathcal{H}}_{int} = -\{\vec{D}_{12}\cdot\vec{\epsilon}_g\,\left(\frac{\hbar\omega_g}{2\epsilon_0 \mathrm{V}}\right)^{1/2}\quad i\quad[\hat{a}_g\,|2\rangle\langle 1|\,e^{-i\omega_g t} + |1\rangle\langle 2|\,\hat{a}_g^{\dagger}\,e^{+i\omega_g t}] +$$

$$\vec{D}_{23}\cdot\vec{\epsilon}_r\,\left(\frac{\hbar\omega_r}{2\epsilon_0 \mathrm{V}}\right)^{1/2}\quad i\quad[\hat{a}_r\,|2\rangle\langle 3|\,e^{-i\omega_r t} + |3\rangle\langle 1|\,\hat{a}_r^{\dagger}\,e^{+i\omega_r t}]\,\} \tag{2.29}$$

Until now we have treated the whole system including light field and ion. The next step would in principle be the calculation of matrix elements such as

$$\langle 2|\otimes\langle n_g|\hat{\mathcal{H}}_{int}|n_g+1\rangle\otimes|1\rangle. \tag{2.30}$$

However, for a laser light source the best description are the coherent photon states. A laser intensity of $1\,\mathrm{mW}$ at $500\,\mathrm{nm}$ corresponds to $\sim 10^{15}$ photons/s which is very large compared to the scattering rate of $\sim 10^7$ photons/s. That means that, when the ion is excited and one photon is removed from the laser beam, the energy of the laser beam changes only by a negligible amount. This is the reason why we assume that the light fields remain in the same coherent state before and after the interaction, which means that we neglect the effect of the interaction on the light field itself. In the limit of large photon numbers the quantum mechanical coherent state has the same effect as a classical monochromatic wave. Therefore we assume constant field states $|\alpha_r\rangle$ and $|\alpha_g\rangle$ and substitute the operators $\hat{a}_g$ and $\hat{a}_r$ by their expectation values α_r and α_g. The energy expectation value of the light field is

$$E_{field} = \langle \alpha_g\,\alpha_r|\hat{\mathcal{H}}_{field}|\alpha_g\,\alpha_r\rangle = \hbar\left(\omega_g(|\alpha_g|^2 + 1/2) + \omega_r(|\alpha_r|^2 + 1/2)\right). \qquad (2.31)$$

We are now ready to write the atomic Hamiltonian in matrix representation with respect to the following basis:

$$|a\rangle \quad , \quad a = 1, 2, 3 \Longrightarrow \begin{pmatrix} 1 \\ 0 \\ 0 \end{pmatrix}, \begin{pmatrix} 0 \\ 1 \\ 0 \end{pmatrix}, \begin{pmatrix} 0 \\ 0 \\ 1 \end{pmatrix} \qquad (2.32)$$

$$\mathcal{H}_{atom} = \hbar \begin{pmatrix} \omega_1 & 0 & 0 \\ 0 & \omega_2 & 0 \\ 0 & 0 & \omega_3 \end{pmatrix} \qquad (2.33)$$

The zero point of energy is chosen at the $|2\rangle$ level:

$$\mathcal{H}_{atom} = \hbar \begin{pmatrix} \omega_1 - \omega_2 & 0 & 0 \\ 0 & 0 & 0 \\ 0 & 0 & \omega_3 - \omega_2 \end{pmatrix} \qquad (2.34)$$

The matrix elements of $\hat{\mathcal{H}}_{int}$ with $\hat{a}_g$ and $\hat{a}_r$ replaced by their expectation values are

$$\langle a\,\alpha_r\,\alpha_g|\hat{\mathcal{H}}_{int}|b\,\alpha_g\,\alpha_r\rangle = -\{\vec{D}_{12}\cdot\vec{\epsilon}_g\,\left(\frac{\hbar\omega_g}{2\epsilon_0 V}\right)^{1/2} i[\delta_{a2}\delta_{b1}\alpha_g e^{-i\omega_g t} - \delta_{a1}\delta_{b2}\alpha_g^* e^{+i\omega_g t}] +$$

$$\vec{D}_{23}\cdot\vec{\epsilon}_r\,\left(\frac{\hbar\omega_r}{2\epsilon_0 V}\right)^{1/2} i[\delta_{a2}\delta_{b3}\alpha_r e^{-i\omega_r t} - \delta_{a3}\delta_{b2}\alpha_r^* e^{+i\omega_r t}] \}$$

$$\delta_{ab} = \begin{cases} 1 & \text{if } a = b \\ 0 & \text{otherwise} \end{cases}$$

which, by choosing the phases (equation (2.12))

$$\theta_g = \pi/2 \quad \Rightarrow \quad \alpha_g = i\,|\alpha_g| \tag{2.35}$$
$$\theta_r = \pi/2 \quad \Rightarrow \quad \alpha_r = i\,|\alpha_r| \tag{2.36}$$
$$\tag{2.37}$$

and with the help of equation (2.19), yields

$$\mathcal{H}_{int} = \hbar \begin{pmatrix} 0 & \frac{\Omega_{12}}{2}e^{+i\omega_g t} & 0 \\ \frac{\Omega_{12}}{2}e^{-i\omega_g t} & 0 & \frac{\Omega_{23}}{2}e^{-i\omega_r t} \\ 0 & \frac{\Omega_{23}}{2}e^{+i\omega_r t} & 0 \end{pmatrix} \tag{2.38}$$

$$\hbar\Omega_{12} := \vec{\epsilon}_g \cdot \vec{D}_{12}\ \mathrm{E}_{0g} \tag{2.39}$$

$$\hbar\Omega_{23} := \vec{\epsilon}_r \cdot \vec{D}_{23}\ \mathrm{E}_{0r} \tag{2.40}$$

The quantities Ω_{12} and Ω_{23} are called Rabi frequencies. They denote the strength of the coupling between atom and electric field.

The complete Hamiltonian is finally

$$\mathcal{H} = \hbar \begin{pmatrix} \omega_1 - \omega_2 & \frac{\Omega_{12}}{2}e^{+i\omega_g t} & 0 \\ \frac{\Omega_{12}}{2}e^{-i\omega_g t} & 0 & \frac{\Omega_{23}}{2}e^{-i\omega_r t} \\ 0 & \frac{\Omega_{23}}{2}e^{+i\omega_r t} & \omega_3 - \omega_2 \end{pmatrix} \tag{2.41}$$

2.3 Density operator formalism and spontaneous decay

Until now we have not described the spontaneous decay of excited atomic states. Spontaneous decay is due to the interaction of the ion with the vacuum modes of the light field. With the help of 'Fermi's golden rule', which includes a summation over all available radiation modes the photons can enter after the interaction, it is possible to calculate the decay rates of the atomic levels. The result is [22]:

$$\Gamma_{ab} = \frac{8\pi^2}{3\epsilon_0\hbar\lambda_{ab}^3} \left| \langle a|\vec{D}|b \rangle \right|^2 \tag{2.42}$$

The coupling of the atom to the vacuum modes also produces a shift of the atomic energy levels, called the Lamb-shift [11–13]. This shift is assumed to be already included in the atomic energy eigenvalues.

A correct description of the damping terms due to spontaneous emission and the finite laser linewidth requires in principle the coupling of a subsystem (the atom) to a surrounding heat-bath (the infinite number of light modes). By restricting our attention

to a subsystem and by considering the rest only by its collective effect, we introduce additional classical statistics into our description. The subsystem is no longer in a pure state and must be described with a density operator $\hat{\rho}$. The density operator $\hat{\rho}$ written in the basis $|a\rangle$ is

$$\hat{\rho} = \sum_{a,b=1,2,3} \rho_{ab} |a\rangle\langle b|. \tag{2.43}$$

The elements $\rho_{11} = \langle 1|\rho|1\rangle$, ρ_{22} and ρ_{33} are the expectation values for finding the ion in the states $|1\rangle$, $|2\rangle$ and $|3\rangle$, respectively, such that

$$\mathrm{Trace}(\hat{\rho}) = \rho_{11} + \rho_{22} + \rho_{33} = 1. \tag{2.44}$$

The elements $\langle a|\hat{\rho}|b\rangle$ are called coherences and represent superpositions of quantum mechanical states.

The time evolution of the density operator is governed by the Liouville equation

$$\frac{d\rho}{dt} = -\frac{i}{\hbar}[\mathcal{H}, \rho] + \mathcal{L}_{damp}(\rho) \tag{2.45}$$

where now $\mathcal{L}_{damp}$ includes the damping terms and the first term corresponds to the Schrödinger equation. It can be shown [23] that the operator $\mathcal{L}_{damp}$ has the following general form

$$\mathcal{L}_{damp}(\rho) = -\frac{1}{2} \sum_m [\hat{C}_m^\dagger \hat{C}_m \rho + \rho \hat{C}_m^\dagger \hat{C}_m - 2\hat{C}_m \rho \hat{C}_m^\dagger]. \tag{2.46}$$

The operators $\hat{C}_m$ describe the different dissipative processes:
In the case of the three level atom we have the decay from the P to the S level, described by

$$\hat{C}_{21} = \sqrt{\Gamma_{21}} \, |1\rangle\langle 2| \tag{2.47}$$

and from the P to the D level

$$\hat{C}_{23} = \sqrt{\Gamma_{23}} \, |3\rangle\langle 2|. \tag{2.48}$$

The finite laser linewidths can be introduced by the operators [24]:

$$\hat{C}_{lg} = \sqrt{2\Gamma_{lg}} \, |1\rangle\langle 1| \tag{2.49}$$

$$\hat{C}_{lr} = \sqrt{2\Gamma_{lr}} \, |3\rangle\langle 3| \tag{2.50}$$

Γ_{lg} and Γ_{lr} denote the laser linewidths of the green and the red laser.

The operator $\hat{C}_{21}$ produces in fact the expected damping terms:

$$-\frac{1}{2}[\hat{C}_{21}^\dagger \hat{C}_{21}\rho + \rho\hat{C}_{21}^\dagger \hat{C}_{21} - 2\hat{C}_{21}\rho\hat{C}_{21}^\dagger] = -\Gamma_{21}|2\rangle\langle 2| + \Gamma_{21}|1\rangle\langle 1| - \frac{\Gamma_{21}}{2}(|1\rangle\langle 2| + |2\rangle\langle 1|)$$

$$\Longrightarrow (\frac{d\rho_{22}}{dt})_{damp} = -(\frac{d\rho_{11}}{dt})_{damp} = -\Gamma_{21}\rho_{22}$$

$$(\frac{d\rho_{12}}{dt})_{damp} = -\frac{\Gamma_{21}}{2}\rho_{12}$$

The final step is a transformation into a rotating frame of reference with the operator $\hat{U}$:

$$\hat{U} = e^{-i(\omega_g|1\rangle\langle 1| + \omega_r|3\rangle\langle 3|)\,t} = \sum_{j=1}^{3} e^{-i(\omega_g\delta_{1j} + \omega_r\delta_{3j})\,t}\,|j\rangle\langle j| \tag{2.51}$$

or in matrix notation with respect to the basis $|a\rangle$, $a = 1,2,3$

$$U = \begin{pmatrix} e^{-i\omega_g t} & 0 & 0 \\ 0 & 1 & 0 \\ 0 & 0 & e^{-i\omega_r t} \end{pmatrix} \quad , \quad UU^\dagger = U^\dagger U = 1 \tag{2.52}$$

The density operator $\hat{\rho}$ is transformed according to

$$\rho' = \hat{U}\,\rho\,\hat{U}^\dagger. \tag{2.53}$$

It is shown in Appendix 8.1 that the corresponding transformation for the Hamiltonian is

$$\hat{\mathcal{H}}' = \hat{U}\hat{\mathcal{H}}\hat{U}^\dagger - i\hbar\hat{U}\frac{d\hat{U}^\dagger}{dt}. \tag{2.54}$$

The damping terms remain unchanged.

We finally obtain the following transformed Hamiltonian:

$$\hat{\mathcal{H}}' = \hbar \begin{pmatrix} \omega_g - (\omega_2 - \omega_1) & \frac{\Omega_{12}}{2} & 0 \\ \frac{\Omega_{12}}{2} & 0 & \frac{\Omega_{23}}{2} \\ 0 & \frac{\Omega_{23}}{2} & \omega_r - (\omega_2 - \omega_3) \end{pmatrix} \tag{2.55}$$

and we define the detunings of the lasers relative to the atomic Bohr frequencies:

$$\Delta_g = \omega_g - (\omega_2 - \omega_1) \tag{2.56}$$

$$\Delta_r = \omega_r - (\omega_2 - \omega_3) \tag{2.57}$$

2.4 Coherence, optical pumping and dark resonances

Since the Liouville-equation (2.45) is linear in the components of ρ, it can be transformed into a vector form

$$\vec{\rho} := (\rho_{11}, \rho_{12}, \dots, \rho_{87}, \rho_{88}) \tag{2.58}$$

$$\frac{d\vec{\rho_i}}{dt} = \sum_j \mathrm{M_{ij}} \; \vec{\rho_j} \tag{2.59}$$

where we have introduced the $N^2 \times N^2$ matrix M. These equations are called optical Bloch-equations.

When the initial condition $\rho(0)$ is given, then the solution of (2.59) is

$$\vec{\rho}(t) = \exp(\mathrm{M}\ t) \; \vec{\rho}(0). \tag{2.60}$$

All terms have been introduced in such a way that ρ remains normalized, i.e.

$$\sum_i \rho_{ii}(0) = 1 \Rightarrow \sum_i \rho_{ii}(t) = 1 \quad \forall\, t. \tag{2.61}$$

In order to obtain the steady-state solution ($\rho(\infty) = $ const. $\Rightarrow \dot{\rho} = 0$), one of the optical Bloch-equations has to be replaced by the normalization condition

$$\sum_i \rho_{ii} = 1 \tag{2.62}$$

and a linear equation system has to be solved. The solution is then unique since we have

$$\mathrm{rank}(\mathrm{M}) = \mathrm{N}^2 - 1. \tag{2.63}$$

As an example for the dynamics described by the optical Bloch equations we first consider the effect of optical pumping, which is caracteristic for a three level system in Λ-configuration. Optical pumping occurs when the ion is illuminated only by one laser and the other laser is blocked. When for example the red laser is blocked the ion is optically pumped into the $^2D_{3/2}$-level: After spontaneous decay to the $^2D_{3/2}$-level the ion is trapped in this state and no more fluorescence photons are emitted.

Figure 2.2 shows the time evolution of the system with $\Omega_{23} = 0$. At time t=0 the ion is in its ground state $|1\rangle$. Then the ion is optically pumped via the state $|2\rangle = \;^2P_{1/2}$ to the state $|3\rangle = \;^2D_{3/2}$. An average number of 3.8 photons is emitted during the process which can be easily calculated using $\Gamma_{23} \int_0^\infty \rho_{22}\, dt = 1$.
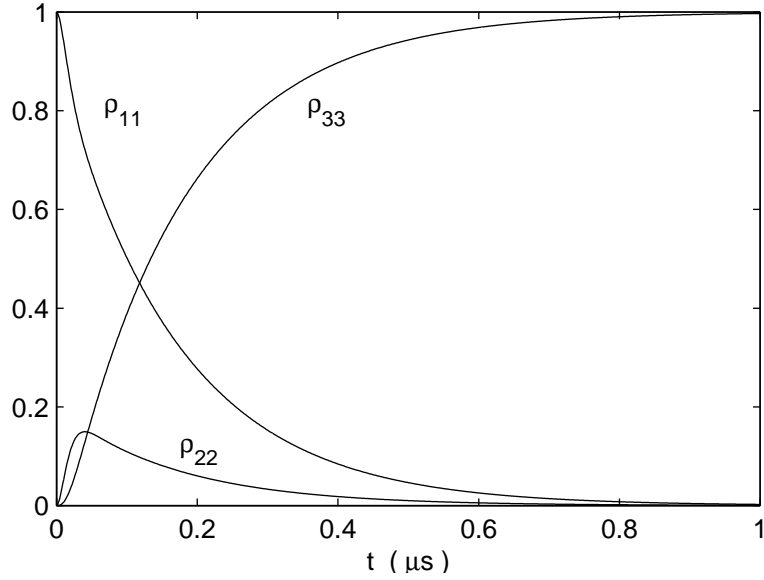
Figure 2.2:   Optical pumping into the state $|3\rangle$.   Parameters: $\Delta_g = \Delta_r = 0$, $\Omega_{12}/2\pi = 10$ MHz, $\Omega_{23} = 0$, $\Gamma_{lg} = \Gamma_{lr} = 0$.
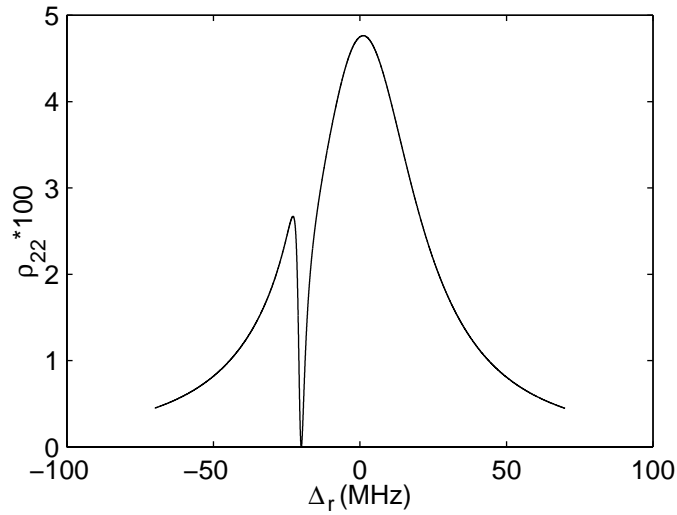
Figure 2.3:   Resonance fluorescence excitation spectrum of a three level system. Parameters: $\Delta_g/2\pi = -20$ MHz, $\Omega_{12}/2\pi = 10$ MHz, $\Omega_{23}/2\pi = 5$ MHz, $\Gamma_{lg} = \Gamma_{lr} = 0$.

The red laser is sometimes called the repumping laser, since in order to observe fluorescence light continously, it is necessary to bring the ion from the D back to the P level. This effect is used in the laboratory to distinguish the ion's fluorescence light from the

background straylight by blocking either the red or the green laser.

As another example figure 2.3 shows a calculated excitation spectrum, i.e the stationary value of ρ_{22} as a function of the red laser detuning. The decay rates used are those of Ba^+: $\Gamma_{21}/2\pi$=15.1 MHz, $\Gamma_{23}/2\pi$=5.3 MHz. When the detunings of the red and the green lasers are equal $\Delta_g = \Delta_r$, which is the condition for a Raman transition between $|1\rangle$ and $|3\rangle$, the P level is not populated and the fluorescence disappears. This effect is called dark resonance. The stationary solutions of the optical Bloch-equations in this case are

$$\rho_{11} = \frac{\Omega_{12}^2}{\Omega_{12}^2 + \Omega_{23}^2} \qquad \rho_{22} = 0 \qquad \rho_{33} = \frac{\Omega_{12}^2}{\Omega_{12}^2 + \Omega_{23}^2} \tag{2.64}$$

$$\rho_{13} = -\frac{\Omega_{12}\Omega_{23}}{\Omega_{12}^2 + \Omega_{23}^2} \qquad \rho_{12} = \rho_{23} = 0 \tag{2.65}$$

which corresponds to a pure state:

$$\hat{\rho} = |\Psi_{\text{dark}}\rangle\langle\Psi_{\text{dark}}| \tag{2.66}$$

$$|\Psi_{\text{dark}}\rangle = \frac{1}{\sqrt{\Omega_{12}^2 + \Omega_{23}^2}}(\Omega_{23}\,|1\rangle - \Omega_{12}\,|3\rangle) \tag{2.67}$$

$$\hat{=} \frac{1}{\sqrt{\Omega_{12}^2 + \Omega_{23}^2}}\begin{pmatrix} \Omega_{23} \\ 0 \\ -\Omega_{12} \end{pmatrix} \tag{2.68}$$

The phenomenon is more easily understood by observing the time-evolution, which is shown in figure 2.4.

We see, that the ion is optically pumped into the superposition state $|\psi_{\text{dark}}\rangle$. This state does not interact with the light field, since

$$\hat{\mathcal{H}}_{int}\,|\Psi_{\text{dark}}\rangle = \hbar\begin{pmatrix} 0 & \frac{\Omega_{12}}{2} & 0 \\ \frac{\Omega_{12}}{2} & 0 & \frac{\Omega_{23}}{2} \\ 0 & \frac{\Omega_{23}}{2} & 0 \end{pmatrix}\begin{pmatrix} \Omega_{23} \\ 0 \\ -\Omega_{12} \end{pmatrix} = 0 \tag{2.69}$$

and consequently the ion is transparent.

Any relative phase fluctuations between the two lasers disturb the perfect superposition of the states $|1\rangle$ and $|3\rangle$. Indeed, we can show that the damping terms we have added in order to describe the finite laser linewidths (eqns. (2.49),(2.50)), lead to a decay of the coherences ρ_{12} and ρ_{23}:

$$-\frac{1}{2}[\hat{C}_{lg}^\dagger\hat{C}_{lg}\rho + \rho\hat{C}_{lg}^\dagger\hat{C}_{lg} - 2\hat{C}_{lg}\rho\hat{C}_{lg}^\dagger] = -\Gamma_{lg}(|2\rangle\langle1| + |1\rangle\langle2|) \tag{2.70}$$

$$\Longrightarrow (\frac{d\rho_{12}}{dt})_{damp} = -\Gamma_{lg}\rho_{12} \tag{2.71}$$
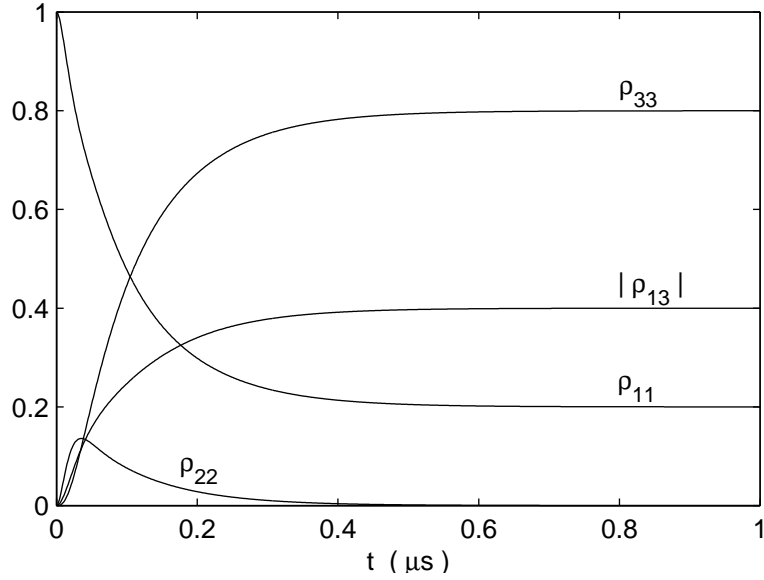
Figure 2.4: Dark resonance: Optical pumping into the superposition state. Parameters: $\Delta_g = \Delta_r=0$, $\Omega_{12}/2\pi=10$ MHz, $\Omega_{23}/2\pi=5$ MHz, $\Gamma_{lg} = \Gamma_{lr}=0$.

and similarly

$$(\frac{d\rho_{23}}{dt})_{damp} = -\Gamma_{lr}\rho_{23}. \tag{2.72}$$

The probability of finding the ion in the excited state $|2\rangle$ is not zero and the fluorescence does not vanish completely. Figure 2.5 illustrates the dependence of the depth of the dark resonance on the laser linewidths.
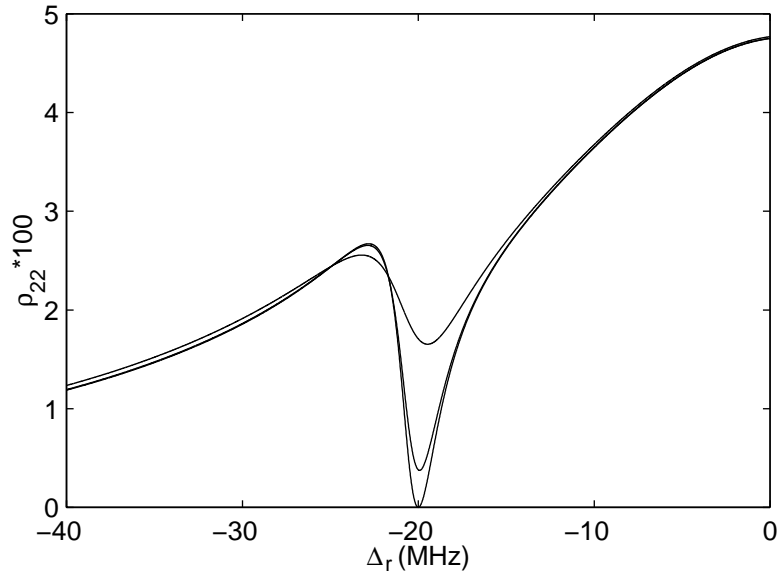
Figure 2.5: Depth of dark resonances for increasing laserlinewidths $\Gamma_{lg} = \Gamma_{lr} = \Gamma_l/2$. Parameters: $\Delta_g/2\pi$=-20 MHz, $\Omega_{12}/2\pi$=10 MHz, $\Omega_{23}/2\pi$=5 MHz, $\Gamma_{lg} = \Gamma_{lr}$=0, 50 kHz, 500 kHz.

19

3 The eight-level system

3.1 Splitting of the energy levels in an external magnetic field

After having discussed the basic concepts of the atom light interaction, we concentrate on the additional effect due to the Zeeman splitting of the atomic energy levels in an external magnetic field.

Without a magnetic field each of the three states $^2S_{1/2}$, $^2P_{1/2}$ and $^2D_{3/2}$ consists of a set of degenerate substates which are described by the magnetic quantum number m_j. We have to consider a total of eight levels. The excitation of these substates depends on the polarization of the laser light fields: When the Ba^+ ion is illuminated by two lasers with linear polarisation only transitions with $\Delta m_j = 0$ can be excited. The ion is optically pumped into the $m_j = \pm 3/2$ states of the $^2D_{3/2}$ level. They are populated via spontaneous decay and cannot be excited by the linear polarized lasers [25, 26].

Optical pumping can be prevented by applying a homogenous magnetic field whose direction is not parallel to the polarization direction of the light fields. However, the magnetic field splits up the energy levels due to the Zeeman effect by an amount [22]

$$\Delta E = m_j g_j \mu_B |\vec{B}| \tag{3.1}$$

or in frequencies

$$\Delta \omega = m_j g_j u \tag{3.2}$$

where we have introduced the quantity

$$u = \frac{\mu_B |\vec{B}|}{\hbar}. \tag{3.3}$$

The Landé factors g_j are calculated by the formula

$$g_j = \frac{J(J+1) + S(S+1) - L(L+1)}{2J(J+1)} \tag{3.4}$$
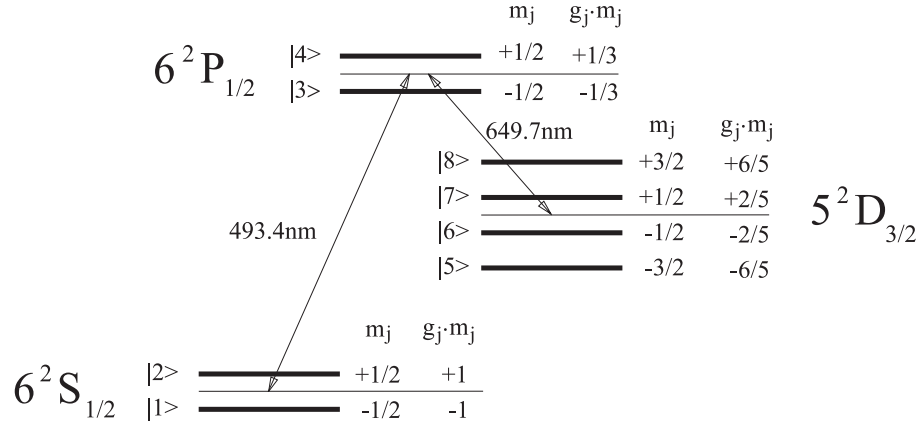
Figure 3.1: Fine structure level scheme of $^{138}\mathrm{Ba}^+$ with Zeeman splitting

which yields in our case

$$g_j(\,^2S_{1/2}) = 2 \qquad g_j(\,^2P_{1/2}) = \tfrac{2}{3} \qquad g_j(\,^2D_{3/2}) = \tfrac{4}{5}. \tag{3.5}$$

The level scheme of $^{138}Ba^+$ with Zeemann splitting is presented in figure 3.1 where the numbering of the atomic basis vectors is also indicated.

The atomic Hamiltonian we obtain for the eight level system is

$$
\begin{aligned}
\hat{\mathcal{H}}_{atom} &= \sum_{a=1}^{8} \hbar\omega_a |a\rangle\langle a| = \\
&= \hbar(\omega_S - u)\,|1\rangle\langle 1| + \hbar(\omega_S + u)\,|2\rangle\langle 2| + \\
&\quad + \hbar(\omega_P - \frac{1}{3}u)\,|3\rangle\langle 3| + \hbar(\omega_P + \frac{1}{3}u)\,|4\rangle\langle 4| + \\
&\quad + \hbar(\omega_D - \frac{6}{5}u)\,|5\rangle\langle 5| + \cdots + \hbar(\omega_D + \frac{6}{5}u)\,|8\rangle\langle 8|
\end{aligned}
\tag{3.6}
$$

3.2   Matrix elements of the interaction Hamiltonian

In view of our experimental setup we make the following simplifications: The magnetic field $\vec{B}$ is assumed to be oriented along the z-axis, which defines the quantization axis. The two light beams propagate in y-direction and we assume them to have the same polarization vector in the x-z-plane:

$$\vec{\epsilon} = \vec{\epsilon}_g = \vec{\epsilon}_r = \begin{pmatrix} \sin(\alpha) \\ 0 \\ \cos(\alpha) \end{pmatrix} \tag{3.7}$$

Hence α is the angle between magnetic field and polarization direction of the lasers. The electric field operators are the same as defined in equation (2.19).

The dipole operator becomes more complex:

$$
\begin{aligned}
\vec{D} = &\vec{D}_{13} \, |1\rangle\langle 3| + \vec{D}_{13}^* \, |3\rangle\langle 1| + \vec{D}_{14} \, |1\rangle\langle 4| + \vec{D}_{14}^* \, |4\rangle\langle 1| + \\
&+\vec{D}_{35} \, |3\rangle\langle 5| + \vec{D}_{35}^* \, |5\rangle\langle 3| + \cdots \\
&\vec{D}_{ab} = \langle a|e\vec{r}|b\rangle
\end{aligned}
\tag{3.8}
$$

and we obtain the following interaction Hamiltonian:

$$
\begin{aligned}
\hat{\mathcal{H}}_{int} = -\Big\{ \, &(\frac{\hbar\omega_g}{2\epsilon_0 V})^{1/2} i \, [\, (\vec{D}_{13}^* \, |3\rangle\langle 1| + \vec{D}_{14}^* \, |4\rangle\langle 1| + \cdots) \, \hat{a}_g e^{-i\omega_g t} \\
&-(\vec{D}_{13} \, |1\rangle\langle 3| + \vec{D}_{14} \, |1\rangle\langle 4| + \cdots) \, \hat{a}_g^\dagger e^{+i\omega_g t}] \\
+&(\frac{\hbar\omega_r}{2\epsilon_0 V})^{1/2} i \, [\, (\vec{D}_{35} \, |3\rangle\langle 5| + \vec{D}_{36} \, |3\rangle\langle 6| + \cdots) \, \hat{a}_r e^{-i\omega_r t} \\
&-(\vec{D}_{35}^* \, |5\rangle\langle 3| + \vec{D}_{36}^* \, |6\rangle\langle 3| + \cdots) \, \hat{a}_r^\dagger e^{+i\omega_r t}] \, \Big\} \cdot \vec{\epsilon}
\end{aligned}
\tag{3.9}
$$

In the next step we calculate the matrix elements of the dipole operator $\vec{D}$. Therefore the position operators x,y,z must be expressed with the help of spherical harmonics Y_l^m.

$$
x = \frac{1}{\sqrt{2}} e \sqrt{\frac{4\pi}{3}} r (Y_1^{-1} - Y_1^1) = \frac{1}{\sqrt{2}}(Q_1^{-1} - Q_1^1)
\tag{3.10}
$$

$$
y = \frac{i}{\sqrt{2}} e \sqrt{\frac{4\pi}{3}} r (Y_1^{-1} - Y_1^1) = \frac{i}{\sqrt{2}}(Q_1^{-1} - Q_1^1)
\tag{3.11}
$$

$$
z = e \sqrt{\frac{4\pi}{3}} r Y_1^0 = Q_1^0.
\tag{3.12}
$$

The electric multipole operators are defined as in [27]:

$$
Q_l^m(r) = e \sqrt{\frac{4\pi}{2l+1}} \, r^l Y_l^m(\theta,\phi)
\tag{3.13}
$$

Q_0^0 is the total charge of the system, Q_1^m, m=-1,0,1 is the electric dipole operator ,Q_2^m the electric quadrupole operator . . . . We consider only electric dipole transitions.

The matrix element of the dipole operator

$$
\langle a|Q_1^m|b\rangle = \langle n_a L_a S_a J_a m_{J_a}|Q_1^m|n_b L_b S_b J_b m_{J_b}\rangle
\tag{3.14}
$$

is determined by first decomposing the coupling between spin and orbital momenta $\vec{S}$ and $\vec{L}$.

$$\langle a|Q_1^m|b\rangle = \sum_{m_{L_a} \, m_{S_a}} \sum_{m_{L_b} \, m_{S_b}} \langle L_a S_a m_{L_a} m_{S_a}|J_a m_{J_a}\rangle \langle L_b S_b m_{L_b} m_{S_b}|J_b m_{J_b}\rangle$$

$$\langle n_a L_a m_{L_a}|Q_1^m|n_b L_b m_{L_b}\rangle \underbrace{\langle S_a m_{S_a}|S_b m_{S_b}\rangle}_{\delta_{m_{S_a} \, m_{S_b}}} \quad (3.15)$$

with $S_a = S_b = S = 1/2$ for the states $^2S_{1/2}$, $^2P_{1/2}$ and $^2D_{3/2}$ and $m_{S_a} = m_{S_b} = m_S$ since Q_1^m (equation(3.13)) does not operate on spin-eigenstates.

Then the theorem of Wigner-Eckhart is employed [27]:

$$\langle n_a L_a m_{L_a}|Q_1^m|n_b L_b m_{L_b}\rangle = \frac{1}{\sqrt{2L_a+1}}\langle L_b, 1, m_{L_b}, m|L_a m_{L_a}\rangle\langle n_a L_a\|Q_1\|n_b L_b\rangle. \quad (3.16)$$

The matrix element $\langle a|Q_1^m|b\rangle$ is obtained as the product of three Clebsch-Gordon-coefficients and the reduced matrix element $\langle n_a L_a\|Q_1\|n_b L_b\rangle$, that characterizes a pair of fine-structure levels and does not depend on the magnetic quantum numbers m_j. In the case of $^{138}Ba^+$ there are two of these quantities: We designate them as d_g for the $^6S_{1/2} \Leftrightarrow {}^6P_{1/2}$ transition and d_r for the $^6P_{1/2} \Leftrightarrow {}^2D_{3/2}$ transition.

The result of the calculation of the dipole operator matrix elements is condensed in appendix 8.2. It reflects the selection rules for transitions between Zeeman sublevels: $\Delta m_j = 0, \pm 1$. We are then able to calculate the matrix elements of the interaction Hamiltonian $(\hat{\mathcal{H}}_{int})_{ab} = \langle a|\hat{\mathcal{H}}_{int}|b\rangle$:

$$(\hat{\mathcal{H}}_{int})_{13} = \Omega_g \frac{1}{\sqrt{3}} \cos(\alpha)e^{+i\omega_g t} \qquad (\hat{\mathcal{H}}_{int})_{14} = -\Omega_g \frac{1}{\sqrt{3}} \sin(\alpha)e^{+i\omega_g t} \qquad (3.17)$$

$$(\hat{\mathcal{H}}_{int})_{23} = -\Omega_g \frac{1}{\sqrt{3}} \sin(\alpha)e^{+i\omega_g t} \qquad (\hat{\mathcal{H}}_{int})_{23} = -\Omega_g \frac{1}{\sqrt{3}} \sin(\alpha)e^{+i\omega_g t} \qquad (3.18)$$

$$(\hat{\mathcal{H}}_{int})_{53} = -\Omega_r \frac{1}{2} \sin(\alpha)e^{+i\omega_r t} \qquad (\hat{\mathcal{H}}_{int})_{54} = 0 \qquad (3.19)$$

$$(\hat{\mathcal{H}}_{int})_{63} = -\Omega_r \frac{1}{\sqrt{3}} \cos(\alpha)e^{+i\omega_r t} \qquad (\hat{\mathcal{H}}_{int})_{64} = -\Omega_r \frac{1}{2\sqrt{3}} \sin(\alpha)e^{+i\omega_r t} \qquad (3.20)$$

$$(\hat{\mathcal{H}}_{int})_{73} = +\Omega_r \frac{1}{2\sqrt{3}} \sin(\alpha)e^{+i\omega_r t} \qquad (\hat{\mathcal{H}}_{int})_{74} = -\Omega_r \frac{1}{\sqrt{3}} \sin(\alpha)e^{+i\omega_r t} \qquad (3.21)$$

$$(\hat{\mathcal{H}}_{int})_{83} = 0 \qquad (\hat{\mathcal{H}}_{int})_{84} = +\Omega_r \frac{1}{2} \sin(\alpha)e^{+i\omega_r t} \qquad (3.22)$$

where the Rabi frequencies Ω_g and Ω_r have been introduced:

$$\hbar\Omega_g := \frac{E_{0g}\, d_g}{2} \tag{3.23}$$

$$\hbar\Omega_r := \frac{E_{0r}\, d_r}{2} \tag{3.24}$$

This definition is different from that of the Rabi frequencies introduced for the three level system (equations (2.39), (2.40)). The phase convention is the same as in equations (2.35), (2.36).

The Hamiltonian still contains terms oscillating with the light frequencies ω_g and ω_r. These terms are removed with the help of the transformation into a rotating frame of reference (equations(2.53), (2.54)). The operator U for the eight level system is

$$U = e^{-i[\omega_r(|5\rangle\langle5|+\cdots+|8\rangle\langle8|)+\omega_g(|1\rangle\langle1|+|2\rangle\langle2|)]\,t}. \tag{3.25}$$

The decay rates of the Zeeman sublevels are calculated using equation (2.42).

$$\Gamma_{ab} = \frac{8\pi^2}{3\epsilon_0\hbar\lambda_{ab}^3}\left|\langle a|\vec{D}|b\rangle\right|^2 \tag{3.26}$$

They are related to the overall decay rates of the fine structure levels by

$$\Gamma_{SP} = \Gamma_{31} + \Gamma_{32} = \frac{8\pi^2}{3\epsilon_0\hbar\lambda_g^3}\left(\left|\langle 3|\vec{D}|1\rangle\right|^2 + \left|\langle 3|\vec{D}|2\rangle\right|^2\right) \tag{3.27}$$

$$= \Gamma_{41} + \Gamma_{42} = \frac{8\pi^2}{3\epsilon_0\hbar\lambda_g^3}\left(\left|\langle 4|\vec{D}|1\rangle\right|^2 + \left|\langle 4|\vec{D}|2\rangle\right|^2\right) \tag{3.28}$$

$$\Gamma_{PD} = \Gamma_{35} + \Gamma_{36} + \Gamma_{37} = \frac{8\pi^2}{3\epsilon_0\hbar\lambda_r^3}\left(\sum_{k=5}^{8}\left|\langle 3|\vec{D}|k\rangle\right|^2\right) \tag{3.29}$$

$$= \Gamma_{46} + \Gamma_{47} + \Gamma_{48} = \frac{8\pi^2}{3\epsilon_0\hbar\lambda_r^3}\left(\sum_{k=5}^{8}\left|\langle 4|\vec{D}|k\rangle\right|^2\right) \tag{3.30}$$

Hence, the decay rates from the P to the S sublevels are

$$\Gamma_{31} = \Gamma_{42} = \Gamma_{SP}\frac{\left|\langle 3|\vec{D}|1\rangle\right|^2}{d_g^2} = \frac{1}{3}\Gamma_{SP} \tag{3.31}$$

$$\Gamma_{32} = \Gamma_{41} = \frac{2}{3}\Gamma_{SP} \tag{3.32}$$

and from the P to the D sublevels:

$$\Gamma_{35} = \Gamma_{48} = \frac{1}{2}\Gamma_{PD} \qquad \Gamma_{36} = \Gamma_{47} = \frac{1}{3}\Gamma_{PD} \tag{3.33}$$

$$\Gamma_{37} = \Gamma_{46} = \frac{1}{6}\Gamma_{PD} \qquad \Gamma_{38} = \Gamma_{45} = 0 \tag{3.34}$$

The damping terms are introduced in the same way as in chapter 2 (equation (2.46)) with appropriate operators C_m. In the case of Zeeman-split multilevel systems this must be done with particular care, in order to take into account the decay of the Zeeman coherences [24].

$$C_1 = \sqrt{\frac{2}{3}\Gamma_{PS}}\,|1\rangle\langle 4| \tag{3.35}$$

$$C_2 = \sqrt{\frac{2}{3}\Gamma_{PS}}\,|2\rangle\langle 3| \tag{3.36}$$

$$C_3 = \sqrt{\frac{1}{3}\Gamma_{PS}}\,(|1\rangle\langle 3| - |2\rangle\langle 4|) \tag{3.37}$$

This operator produces terms similar to equation (2.51) and one additional term that leads to a decay of the excited state Zeeman coherence ρ_{12} into a ground state Zeeman coherence:

$$(\frac{d\rho_{12}}{dt})_{damp} = -\sqrt{\Gamma_{31}\Gamma_{24}}\rho_{34} = -\frac{1}{3}\Gamma_{SP}\rho_{34}. \tag{3.38}$$

The other Zeeman coherences decay in a similar way [24, 25]:

$$(\frac{d\rho_{56}}{dt})_{damp} = (\frac{d\rho_{78}}{dt})_{damp} = \frac{1}{\sqrt{12}}\Gamma_{PD}\rho_{34} \tag{3.39}$$

$$(\frac{d\rho_{67}}{dt})_{damp} = \frac{1}{3}\Gamma_{PD}\rho_{34} \tag{3.40}$$

Therefore the operators C_m have the following form:

$$C_4 = \sqrt{\frac{\Gamma_{PD}}{2}}\,|5\rangle\langle 3| + \sqrt{\frac{\Gamma_{PD}}{6}}\,|6\rangle\langle 4| \tag{3.41}$$

$$C_5 = \sqrt{\frac{\Gamma_{PD}}{6}}\,|7\rangle\langle 3| + \sqrt{\frac{\Gamma_{PD}}{2}}\,|8\rangle\langle 4| \tag{3.42}$$

$$C_6 = \sqrt{\frac{\Gamma_{PD}}{3}}\,(|6\rangle\langle 3| + |7\rangle\langle 4|). \tag{3.43}$$

Finally the operators describing the effect of the finite laser linewidths are added:

$$C_7 = \sqrt{2\Gamma_{lg}}\,(|1\rangle\langle 1| + |2\rangle\langle 2|) \tag{3.44}$$

$$C_8 = \sqrt{2\Gamma_{lr}}\,(|5\rangle\langle 5| + |6\rangle\langle 6| + |7\rangle\langle 7| + |8\rangle\langle 8|). \tag{3.45}$$

3.3 The parameters of the equations

After the Hamiltonian and the damping operators have been determined, it is possible to write the optical Bloch equations for the Barium ion. As in the case of the three

level system the equations are transformed into a matrix form (equation (2.59)), with M being a 64×64 matrix. The detailed procedure and the corresponding computer program are described in appendix 8.3. The matrix M contains the following experimental parameters:

- **The intensities I_g and I_r of the green and the red laser**
  In the course of the calculation of the interaction Hamiltonian matrix elements the Rabi frequencies Ω_g and Ω_r with $\Omega = \frac{E_o d}{2\hbar}$ were introduced as model parameters. They are not easily measurable physical quantities but can be related to the light intensities at the position of the ion:

$$I_g = \frac{1}{2}c\epsilon_0 E_{0g}^2 \tag{3.46}$$

$$I_r = \frac{1}{2}c\epsilon_0 E_{0r}^2. \tag{3.47}$$

The reduced matrix elements d_g and d_r can be expressed with the decay rates of the fine structure levels Γ_{SP} and Γ_{PD} using equations (3.27)-(3.30) and the dipole operator matrix elements summarized in appendix 8.2:

$$\Gamma_{SP} = \frac{8\pi^2}{3\epsilon_0\hbar\lambda_g^3}d_g^2 \tag{3.48}$$

$$\Gamma_{PD} = \frac{8\pi^2}{3\epsilon_0\hbar\lambda_r^3}d_r^2. \tag{3.49}$$

Hence:

$$I_g(\Omega_g) = \frac{16\pi^2}{3}c\hbar\frac{1}{\lambda_g^3\Gamma_g}\Omega_g^2 \tag{3.50}$$

$$I_g(\Omega_r) = \frac{16\pi^2}{3}c\hbar\frac{1}{\lambda_r^3\Gamma_r}\Omega_r^2. \tag{3.51}$$

Finally we define the following saturation parameters:

$$S_g = \frac{\Omega_g}{\Gamma_g} \tag{3.52}$$

$$S_r = \frac{\Omega_r}{\Gamma_r}. \tag{3.53}$$

They are helpful to distinguish a strong (S>1) from a weak (S<1) excitation that determines, e.g., the spectral shape of the resonance fluorescence excitation spectrum. They should, however, not be compared to saturation parameters introduced in two level systems because in a three level system strong excitation

on one transition leads to optical pumping rather than to saturation (as in a two level system).

When the saturation parameters are known the intensity of the laser can be calculated using

$$I(S)\left(\frac{mW}{cm^2}\right) = 1.0456 \times 10^9 \frac{\Gamma\,(MHz)}{\lambda^3\,(nm^3)}\,S^2 \tag{3.54}$$

which yields for the Barium transitions:

$$I_g(S_g) = 131 \cdot S_g^2 \frac{mW}{cm^2} \tag{3.55}$$

$$I_r(S_r) = 20.2 \cdot S_r^2 \frac{mW}{cm^2} \tag{3.56}$$

- **The detunings of the lasers** relative to the atomic Bohr frequencies at $|\vec{B}| = 0$

$$\Delta_g = \omega_g - (\omega_P - \omega_S) \tag{3.57}$$

$$\Delta_r = \omega_r - (\omega_P - \omega_D) \tag{3.58}$$

ω_S, ω_P and ω_D have been introduced in equation (3.6).

- **The magnetic field**
  which enters into the model through the quantity

$$u = \frac{\mu_B |\vec{B}|}{\hbar} \qquad \frac{\mu_B}{h} = 0.14 \frac{MHz}{G}. \tag{3.59}$$

u is in the order of a few MHz and $|\vec{B}|$ in the order of some ten Gauss.

- **The angle α between the magnetic field and the polarization of the light fields**

- **The linewidths Γ_{lg} and Γ_{lr} of the two lasers**

The ion is, in principle, fully characterized only by its decay constants. The same model can therefore be also applied to other ions with the same level structure (see appendix 8.5).

3.4   Discussion of the solution

The oscillating electric dipoles of the excited ion are the light sources studied in our experiment. Their effect is best described by the electric field operators E^+, E^- at the detector position [21], which is in our case perpendicular to the laser beam in z-direction (i.e. the direction of the magnetic field). Only the oscillating dipoles in x- and y-direction contribute to the observed electric field operator [25]:

$$\hat{\vec{E}}^- \propto \omega_g^2 \ (\ \vec{D}_{41} \ |4\rangle\langle 1| + \vec{D}_{32} \ |3\rangle\langle 2| \ ) + \tag{3.60}$$

$$\omega_r^2 \ (\ \vec{D}_{48} \ |4\rangle\langle 8| + \vec{D}_{46} \ |4\rangle\langle 6| + \tag{3.61}$$

$$\vec{D}_{37} \ |3\rangle\langle 7| + \vec{D}_{35} \ |3\rangle\langle 5| \ ). \tag{3.62}$$

With this field operator it is possible to calculate the intensity $I(t)$ and the photon counting rate, the degree of second order coherence $g^{(2)}(\tau)$ and the degree of first order coherence $g^{(1)}(\tau)$ of the resonance fluorescence, which also permits the calculation of the spectrum of resonance fluorescence [21]:

$$\hat{I}(t) = 2\epsilon_0 c \hat{E}^-(t)\hat{E}^+(t) \tag{3.63}$$

$$g^{(1)}(t_1, t_2) = \frac{\langle \hat{E}^-(t_1)\hat{E}^+(t_2)\rangle}{\sqrt{\langle \hat{I}(t_1)\rangle\langle \hat{I}(t_2)\rangle}} \tag{3.64}$$

$$g^{(2)}(t_1, t_2) = \frac{\langle \hat{E}^-(t_1)\hat{E}^-(t_2)\hat{E}^+(t_1)\hat{E}^+(t_2)\rangle}{\langle \hat{I}(t_1)\rangle\langle \hat{I}(t_2)\rangle}. \tag{3.65}$$

The expectation values in the above formulas are calculated with the atomic density operator:

$$\langle \hat{O}\rangle(t) = \text{Trace}\left(\hat{\rho}(\text{t})\hat{O}\right). \tag{3.66}$$

We concentrate here on the resonance fluorescence excitation spectrum described by $\rho_{33}(\infty) + \rho_{44}(\infty)$ as a function of the green or red laser detuning. It can be shown [25] that the photon counting rate $\frac{\langle n\rangle}{T}$ in the steady state regime is proportional to the probability of finding the ion in its excited states

$$\frac{\langle n\rangle}{T} \propto \rho_{33}(\infty) + \rho_{44}(\infty) \tag{3.67}$$

similar to equation (2.3).

In figure 3.2 a spectrum with four dark resonances is plotted. Dark resonances occur when the detunings with respect to certain Zeeman sublevels are equal:

$$\Delta_g - \Delta_r = \pm\frac{1}{5}u, \ \pm\frac{3}{5}u, \ \pm\frac{7}{5}u, \ \pm\frac{11}{5}u. \tag{3.68}$$
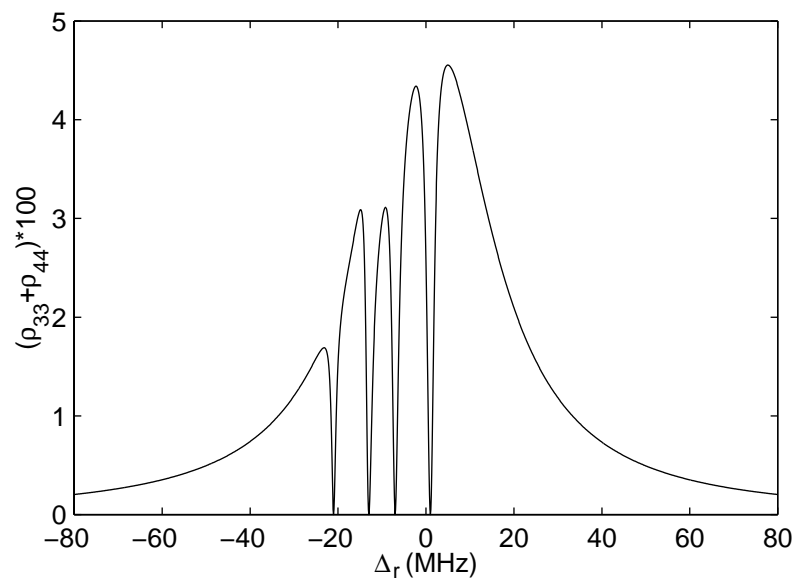
Figure 3.2: Excitation spectrum with $\alpha = 90°$. Parameters: $\Delta_g/2\pi$=-10 MHz, S_g=0.5, S_r=1 ,$u/2\pi$=5 MHz, $\Gamma_{lg} = \Gamma_{lr}$=0.
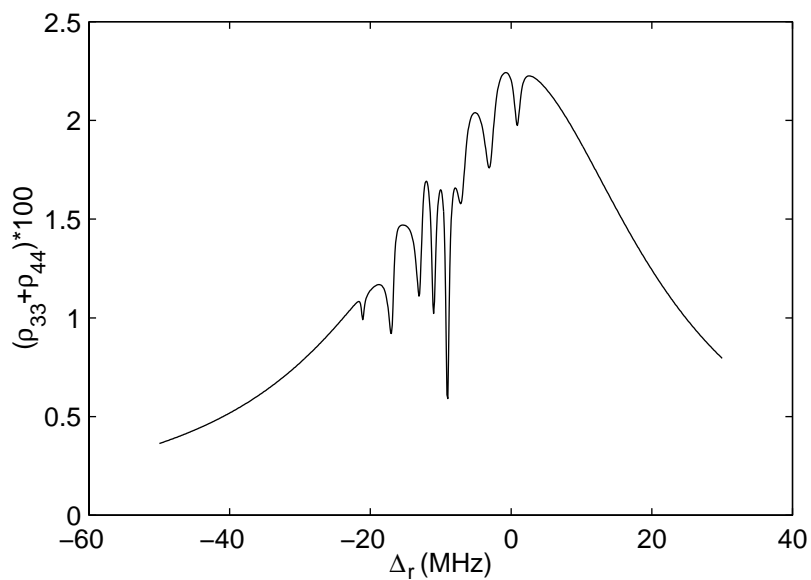
Figure 3.3: Excitation spectrum with $\alpha = 30°$. All eight possible dark resonances appear. Parameters: $\Delta_g/2\pi$=-10 MHz, S_g=0.25 , S_r=1 ,$u/2\pi$=5 MHz, $\Gamma_{lg} = \Gamma_{lr}$=0.

Four of the twelve possible dark resonances are degenerate and therefore a maximum number of eight dark resonances can be observed. Which of these dark resonances appear depends on the angle α between polarization and magnetic field. Figure 3.2 is calculated with $\alpha = 90°$. In this configuration only Zeeman sublevels with $\Delta m_j = \pm 1$ are coupled (equations (3.17)-(3.22)). The four dark resonances are found at $\Delta_r = \Delta_g \pm \frac{3}{5}u$ and $\Delta_r = \Delta_g \pm \frac{11}{5}u$. In figure 3.4 the corresponding coherences ρ_{16}, ρ_{18}, ρ_{25}, ρ_{27} are plotted. At $\Delta_g = \Delta_r - \frac{11}{5}u$ for example the coherence ρ_{18} is resonant, which corresponds to the superpositions of the states $|1\rangle = {}^2S_{1/2}$, $m_j = -1/2$ and $|8\rangle = {}^2D_{3/2}$, $m_j = +3/2$.

When $\alpha = 0°$ only Zeeman transitions with $\Delta m_j = 0$ are excited which leads to optical pumping into the $m_j = \pm 3/2$ states of the ${}^2D_{3/2}$ level, i.e. the steady state solution is $\rho_{33} = \rho_{44} = 0$.

For an arbitrary angle α all eight dark resonances are observed, for example $\alpha = 30°$ in figure 3.3.

In the first two chapters we have both developed the formalism describing the interaction of the lasers with the Ba^+ ion and given interpretations which phenomenons are hidden behind the excitation spectra. Herewith we have created the basis for the comparison of our measurements to the calculations.
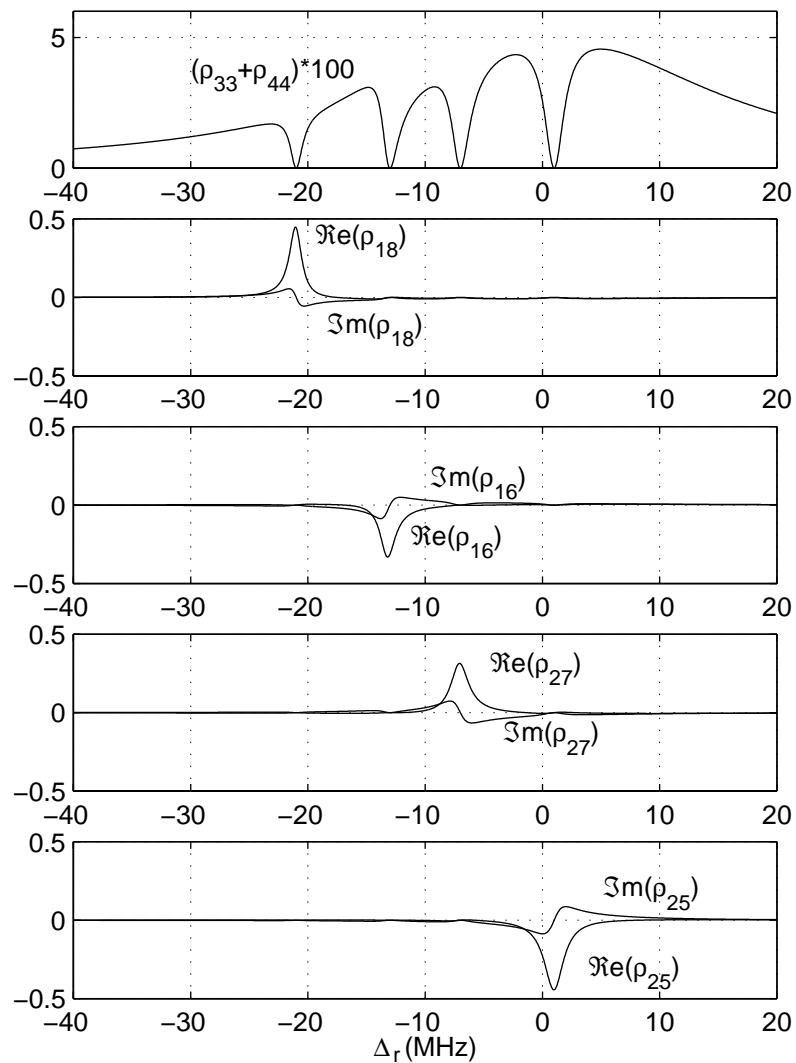
Figure 3.4: Excitation spectrum and coherences ρ_{16}, ρ_{18}, ρ_{25}, ρ_{27} . Parameters: $\alpha = 90°$, $\Delta_g/2\pi$=-10 MHz, S_g=0.5, S_r=1, $u/2\pi$=5 MHz, $\Gamma_{lg} = \Gamma_{lr}$=0.

4 The influence of the ion's motion on the resonance fluorescence

4.1 Setup of a Paul-trap, equations of motion and stable solutions

In order to examine the resonance fluorescence of Ba$^+$ it is necessary to confine one isolated ion for a sufficiently long time to a certain small region in space. This is achieved with a radio-frequency trap, often called Paul trap [28–30].

Figure 4.1: Electrode configuration of a Paul-trap

Figure 4.1 shows a typical electrode configuration, with ring- (radius=r_0) and endcap electrodes (distance=$2z_0$). In an ideal configuration they have the form of rotational hyperboloids. When a potential U_0 is applied between the endcap and the ring the

electro-static potential in the trap center forms a saddle:

$$U(r,z) = \frac{U_0}{R_0^2}(r^2 - 2z^2) \tag{4.1}$$

$$R_0^2 = r_0^2 + 2z_0^2. \tag{4.2}$$

A charged particle will be either confined in the axial direction or in the radial plane. This can be overcome by applying an additional radio-frequency potential to the electrodes

$$U_0 = U_{dc} + U_{ac}\cos(\Omega t) \tag{4.3}$$

where Ω is the trap drive frequency.

The equations of motion for a particle with charge e and mass m under the influence of this potential are:

$$m\frac{d^2r}{dt^2} = -\frac{2e}{R_0^2}\left(U_{dc} - U_{ac}\cos(\Omega t)\right)r \tag{4.4}$$

$$m\frac{d^2z}{dt^2} = +\frac{4e}{R_0^2}\left(U_{dc} - U_{ac}\cos(\Omega t)\right)z \tag{4.5}$$

These equations are Mathieu equations and their solutions may be stable or unstable depending on the parameters. They are usually transformed to their standard form by introducing the following dimensionless quantities:

$$a_z = -2a_r = -\frac{16eU_{dc}}{mR_0^2\Omega^2} \tag{4.6}$$

$$q_z = -2q_r = -\frac{8eU_{ac}}{mR_0^2\Omega^2} \tag{4.7}$$

$$\tau = \frac{\Omega}{2}t \tag{4.8}$$

which yields:

$$\frac{d^2x_i}{d\tau^2} + (a_i - 2q_i\cos(2\tau))\,x_i = 0 \qquad i = r,z \tag{4.9}$$

The experimentally relevant stability region can be found in the literature [29]. When the parameters are chosen inside this region the ion is confined to the trapping region for all times. A general solution is complicated but for $a_i \approx 0$ and $q_i \ll 1$ an approximate solution can be given that reflects the general behavior quite well:

$$x_i = A\left(1 - \frac{q_i}{2}\cos(\Omega t)\right)\cdot\cos(\frac{\beta_i\Omega}{2}t - \varphi_i) \tag{4.10}$$

$$\beta_i = a_i + \frac{1}{2}q_i^2 \tag{4.11}$$

The ion's motion is composed of a slow oscillation, called the secular motion, with frequencies $\beta_i \Omega/2$ and a superimposed fast oscillation at the trap drive frequency Ω with smaller amplitude, called the micromotion.

The micromotion is driven by the oscillating potential and its amplitude is proportional to the distance of the ion from the trap center. The secular motion can be described in terms of a pseudo potential, obtained by averaging the rf-potential over the micromotion period. For characteristic experimental parameters ($R_0^2 \approx 1\,\mathrm{mm}, \mathrm{U_{ac}} \approx 100\,\mathrm{V}$) the potential depth of the trap can reach several $10\,\mathrm{eV}$ which allows the confinement of particles with thermal energy.

The secular motion of the ion can be damped with optical cooling techniques, such as Doppler cooling and side-band cooling. A complete description of laser cooling techniques and their temperature limits can be found in the literature ([29, 31, 32] and the references therein). Cooling to the ground state of the (quantum mechanical) harmonic oscillator has been demonstrated [33]. In our experiment the Barium ion is Doppler-cooled with the laser at $493\,\mathrm{nm}$.

4.2   Bloch equations with a periodic motion of the ion

When the ion moves with the velocity v relative to the light beam the effective laser frequency for the ion is shifted due to the Doppler effect:

$$\omega = \omega_0 \left(1 \pm \frac{v}{c}\right) \frac{1}{\sqrt{1 - \frac{v^2}{c^2}}} \approx \omega_0 \pm kv - \frac{v^2}{2c^2}\omega_0 \tag{4.12}$$

$$k = |\vec{k}| = \frac{\omega_0}{c} \tag{4.13}$$

The second order Doppler shift can be neglected (v $\approx 1\,\mathrm{m/s}$). As we have seen in the previous section the ion's motion is made up of two oscillations with different frequencies, the secular- and the micromotion. The velocity of the secular motion is normally much smaller than that of the micromotion. It is assumed that the frequency shift is dominated by a simple harmonic oscillation at the trap frequency Ω and with velocity amplitude v_0

$$v = v_0 \cos(\Omega t) \tag{4.14}$$

and hence, when the lasers propagate in the same direction:

$$\omega_g = \omega_{g0} + k_g v_0 \cos(\Omega t) \tag{4.15}$$

$$\omega_r = \omega_{r0} + k_r v_0 \cos(\Omega t) \tag{4.16}$$

This leads to a modulation of the detunings (equations (3.57), (3.58)).

$$\Delta_g = \Delta_{g0} + k_g v_0 \cos(\Omega t) \tag{4.17}$$

$$\Delta_r = \Delta_{r0} + k_r v_0 \cos(\Omega t). \tag{4.18}$$

Again, a linear differential equation for the density matrix is obtained, but now the matrix M is a periodic function of time:

$$\frac{d\vec{\rho}}{dt} = M(t)\,\vec{\rho} \tag{4.19}$$

Since M is a linear function of the detunings $\Delta_g(t)$ and $\Delta_r(t)$ it is possible to separate the time dependence:

$$M(t) = M(\Delta_g + k_g v_0 \cos(\Omega t), \Delta_r + k_r v_0 \cos(\Omega t), p) =$$
$$= \underbrace{M(\Delta_g, \Delta_r, p)}_{=:M_0} + \underbrace{(k_g v_0 \,\Delta M_g + k_r v_0 \,\Delta M_r)}_{=:2\,\Delta M} \cos(\Omega t) \tag{4.20}$$

with

$$\Delta M_g = M(1, 0, p) - M(0, 0, p) \tag{4.21}$$

$$\Delta M_r = M(0, 1, p) - M(0, 0, p), \tag{4.22}$$

where p denotes the rest of parameters that determine the matrix M described in 3.3. Hence, we can write:

$$\frac{d\vec{\rho}}{dt} = (M_0 + 2\Delta M\,\cos(\Omega t))\,\vec{\rho}. \tag{4.23}$$

When the initial condition is known, the equation can be numerically integrated, which is shown in figure 4.2 for a three level system. In the limit of long times the solution approaches a stable oscillation with frequency components only at multiples of Ω [26].

$$\vec{\rho}(t) = \sum_{n=-\infty}^{\infty} \vec{\rho}_n e^{in\Omega t} \tag{4.24}$$

It can be shown that this periodic solution of equation (4.23) is unique. We are interested in the time-averaged stationary solution $\vec{\rho}_0 = \frac{1}{\Omega} \int_0^{\Omega} \vec{\rho}(t) dt$.

Equation (4.24) inserted into equation (4.23) yields:

$$(M_0 + in\Omega)\,\vec{\rho}_n + \Delta M\,(\vec{\rho}_{n+1} + \vec{\rho}_{n-1}) = 0 \tag{4.25}$$
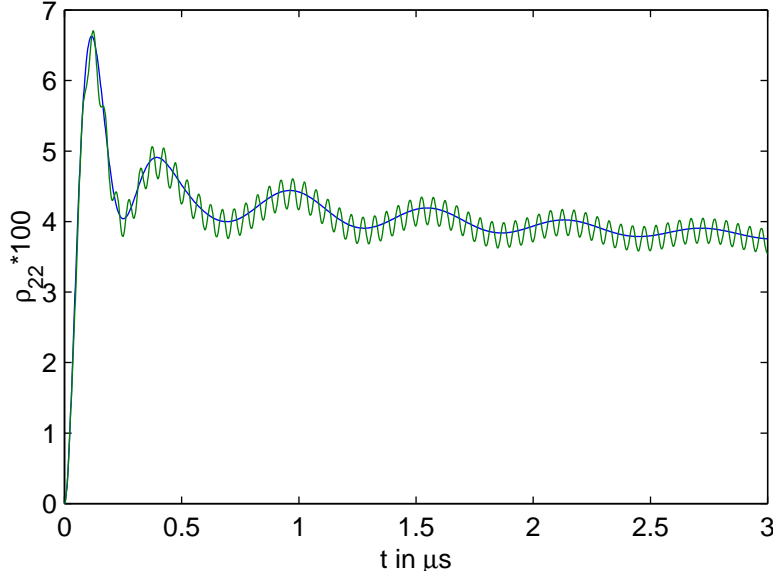
Figure 4.2: Time evolution of the excited state for a three level ion with a periodic motion in the trap. Parameters: $\Omega_{12}/2\pi=10$ MHz, $\Omega_{23}/2\pi=5$ MHz, $\Delta_g/2\pi=$-20 MHz, $\Delta_r/2\pi=$-10 MHz, $\Gamma_{lg} = \Gamma_{lr}=0$, trap frequency $\Omega/2\pi=20$ MHz, velocity amplitude v=0,10 m/s.

In order to obtain an approximate solution it is convenient to introduce the operators S_n^+ and S_n^-. We define them by the following matrix continued fraction

$$S_{n-1}^+ = -(M_0 + in\Omega + \Delta M\, S_n^+)^{-1}\Delta M \qquad n \geq 0 \tag{4.26}$$
$$S_{n+1}^- = -(M_0 + in\Omega + \Delta M\, S_n^-)^{-1}\Delta M \qquad n \leq 0 \tag{4.27}$$

The components $\vec{\rho}_n$ are then calculated by

$$\vec{\rho}_n = S_{n-1}^+ S_{n-2}^+ \ldots S_0^+\, \vec{\rho}_0 \qquad n > 0 \tag{4.28}$$
$$\vec{\rho}_n = S_{n+1}^- S_{n+2}^- \ldots S_0^-\, \vec{\rho}_0 \qquad n < 0 \tag{4.29}$$

or equivalently

$$\vec{\rho}_{n+1} = S_n^+\, \vec{\rho}_n \qquad n \geq 0 \tag{4.30}$$
$$\vec{\rho}_{n-1} = S_n^-\, \vec{\rho}_n \qquad n \leq 0. \tag{4.31}$$

The phase modulation of the light fields creates sidebands to the central laser frequency. The strength of these sidebands is determined by the modulation index $\frac{kv}{\Omega}$. For laser-cooled ions in a Paul trap only a small number of components has to be considered.

The continued fraction therefore starts with $S^+_{n_{max}} = 0$ and $S^-_{n_{max}} = 0$, with $n_{max} \approx \frac{kv}{\Omega}$, and $S^{\pm}_0$ can be calculated. When S^+_0 and S^-_0 are known the solution $\vec{\rho}_0$ is determined with

$$\left(M_0 + \Delta M \left(S^+_0 + S^-_0\right)\right) \vec{\rho}_0 = 0 \qquad (4.32)$$

(equations (4.25), (4.30), (4.31)) and the normalization condition for $\vec{\rho}_0$.

It is easily seen that the components $\vec{\rho}_n$ obtained with this procedure fulfil the equation (4.25) for $-n_{max} \leq n \leq n_{max}$: The definition of S^+_n (equation (4.26)) yields

$$\left(M_0 + in\Omega + \Delta M\, S^+_n\right) S^+_{n-1} + \Delta M = 0. \qquad (4.33)$$

By multiplying this equation with $\vec{\rho}_{n-1}$ we obtain

$$\left(M_0 + in\Omega + \Delta M\, S^+_n\right) \underbrace{S^+_{n-1}\, \vec{\rho}_{n-1}}_{\vec{\rho}_n} + \Delta M\, \vec{\rho}_{n-1} =$$

$$= \left(M_0 + in\Omega\right) \vec{\rho}_n + \Delta M\, \underbrace{S^+_n\, \vec{\rho}_n}_{\vec{\rho}_{n+1}} + \Delta M\, \vec{\rho}_{n-1} = 0 \quad (4.34)$$

which is just equation (4.25). The same is true for S^-_n.
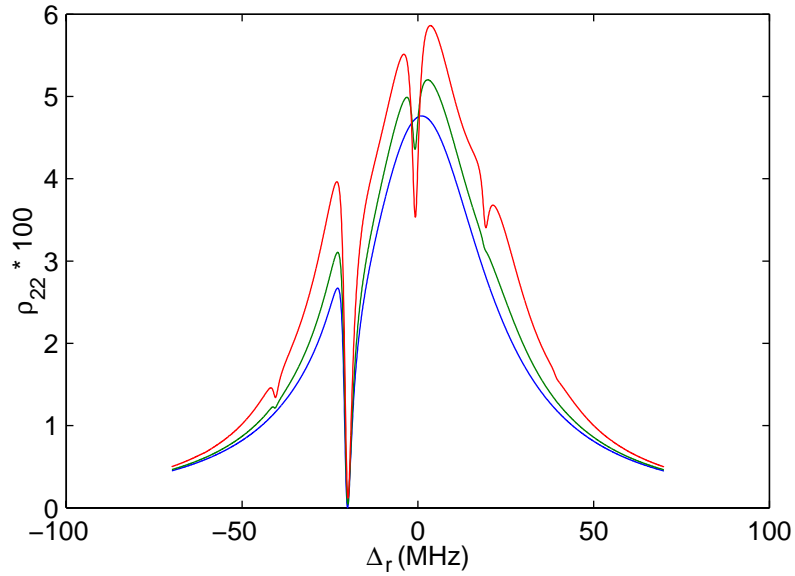
Figure 4.3: Excitation spectrum with sidebands due to the periodical motion. Parameters: $\Omega_{12}/2\pi$=10 MHz, $\Omega_{23}/2\pi$=5 MHz, $\Delta_g/2\pi$=-20 MHz, $\Gamma_{lg} = \Gamma_{lr}$=0, trap frequency $\Omega/2\pi$=20 MHz, velocity amplitude v=0,5,10 m/s.

In Figure 4.3 a resonance fluorescence excitation spectrum is plotted for several velocity amplitudes. It is seen that sidebands of the dark resonance appear that become deeper the higher the velocity is, whereas the depth of the central dark resonance decreases.

5 Experimental setup

The experiment is basically made up of three parts: the two laser light sources, the vacuum vessel with the trap and the photon detection systems which are all presented in this chapter. They have already been characterized and described in detail in particular papers, the laser at 650nm in [34, 35], the laser at 493nm in [36], the vacuum vessel and the optical setup are fully described in [37].

Figure 5.1 shows a schematic overview of the experimental setup with all its components.

5.1   The laser systems

The light at 493 nm is produced by frequency doubling light emitted by a 986 nm laser diode (SDL 6571-J1, P_{max}=150 mW), whereas the light at 650nm is produced directly by a laser diode (SDL 7511-G1, P_{max}=30 mW). The inherent emission bandwidths of laser diodes are in the range of 100 MHz which is too large for precision spectroscopy. In order to obtain coherent superpositions of atomic states necessary for well resolved dark resonances the laser linewidths should be lower than 100 kHz. This is achieved with optical feedback from a grating in the Littman-Metcalf configuration [38] and an additional electronic stabilization.

Both laser diodes are mounted on a temperature stabilized copper block. The light emitted by the diode is collimated to a parallel beam with a lens and then illuminates a grating (1800 lines/mm(red), 1400 lines/mm(infrared)). The light diffracted into the first order is back reflected from a mirror into the laser diode. The optical feedback can be optimized by choosing the angle of incidence on the grating. The mirror can be shifted by applying a high voltage to the piezo ceramic to which it has been glued. The 0th diffraction order is circularized with the help of anamorphic prisms and then coupled out. The flexible setup permits, by tuning and shifting the mirror and by adjusting laser diode current and temperature, selection of the lasing wavelengths.

A Pound-Drever-Hall stabilization scheme [39] is used to lock the laser to a reference cavity. Therefore sidebands to the central laser frequency have to be generated. This
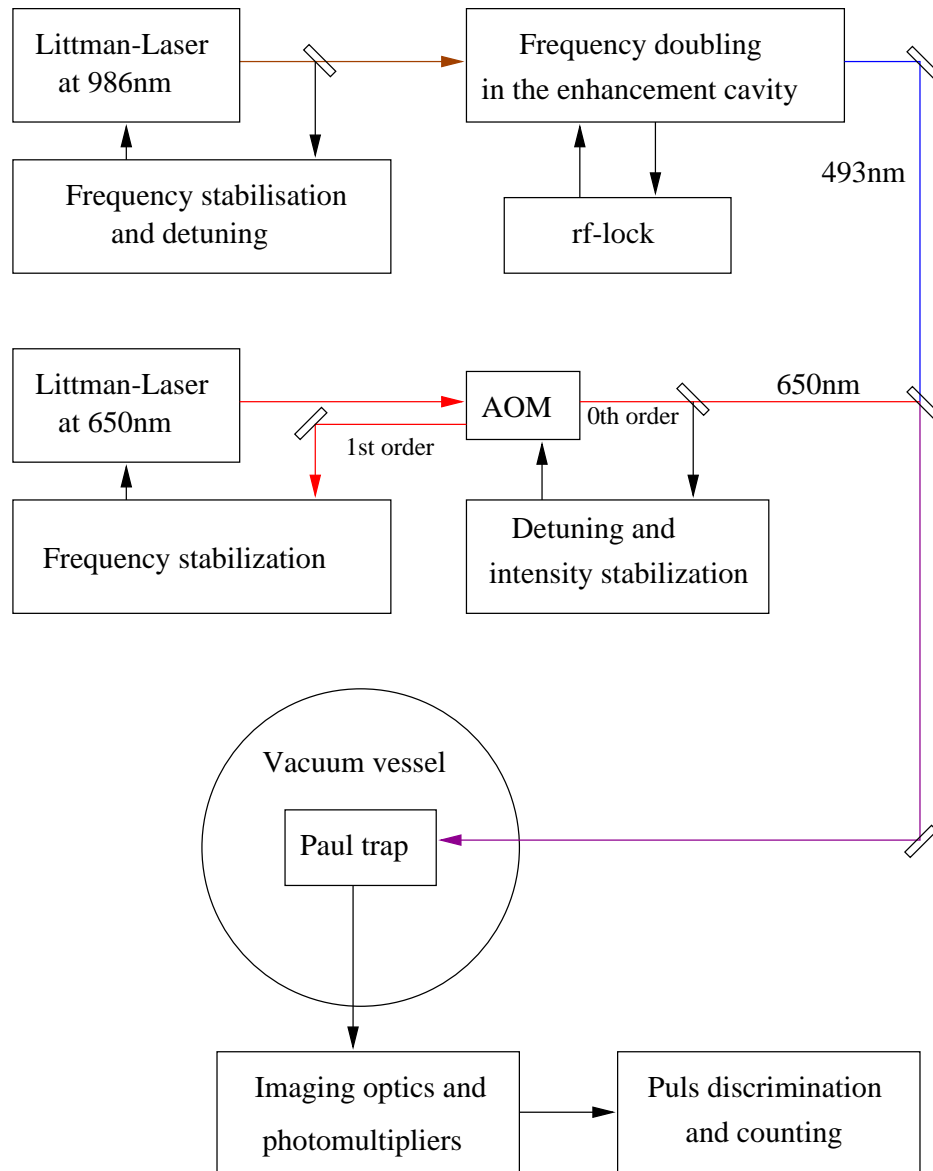
Figure 5.1: Schematic overview of the experimental setup with the two lasers at 493 nm and 650 nm, the vacuum vessel with the trap and the photon detection system.

is done in the case of the infrared diode by directly modulating the current at 16 MHz. The laser at 650nm is focused through an electro-optical-modulator(EOM) to which the 16 MHz modulation frequency is applied.

The light is then coupled into the reference cavity. The back reflected beam is separated at a polarizing beam splitter and analysed with a fast photodiode, whose photo current is demodulated with the 16 MHz reference. When the relative phase is well adjusted a dispersive error signal is obtained that is amplified and fed back to the laser diode current and the piezo voltage.

The cavity used for the laser at 986 nm has a finesse of 1200 and a free spectral range of 730 MHz. One of the mirrors is mounted on a piezo and permits tuning of the cavity and hence the locked laser. A laser linewidth below 30kHz with respect to the reference cavity has been achieved [36].

The light at 986 nm is frequency doubled with the help of a $KNbO_3$ crystal that is placed in the focus of an enhancement resonator. In this resonator the light intensity is enhanced by a factor of 70 which makes it possible to create the first harmonic light wave in the crystal due to its high nonlinear susceptibility. Phase matching of the two waves, fundamental and doubled, is attained by heating the crystal to approximately 35°C. The 16 MHz sidebands are again used in a Pound-Dever-scheme to lock the ring resonator to the infrared laser frequency. When 94 mW of infrared light is coupled into the frequency doubler an output power of up to 60 mW of green laser light can be reached (conversion efficieny $\sim 60\%$) [36].

The setup of the red laser is shown in figure 5.2. In the upper part the components of the Pound-Drever locking scheme can be seen, i.e. the EOM, used to create sidebands to the laser frequency at 16 MHz, the reference cavity, the electronic demodulation and the servo amplifier.

The red laser is not detuned with the help of the reference cavity, but with an acousto-optical-modulator(AOM) that is driven by a precision frequency generator (Marconi frequency generator 2023). Since the diffraction angle changes with frequency, the beam position changes when the laser is detuned. To overcome this effect the diffracted beam is back reflected into the AOM with a lens and a mirror. This double pass setup has the additional advantage of doubling the detuning range. The back reflected beam is separated with a quarter wave plate and a polarizing beam splitter and subsequently used for frequency stabilization. The setup is shown in the lower part of figure 5.2.
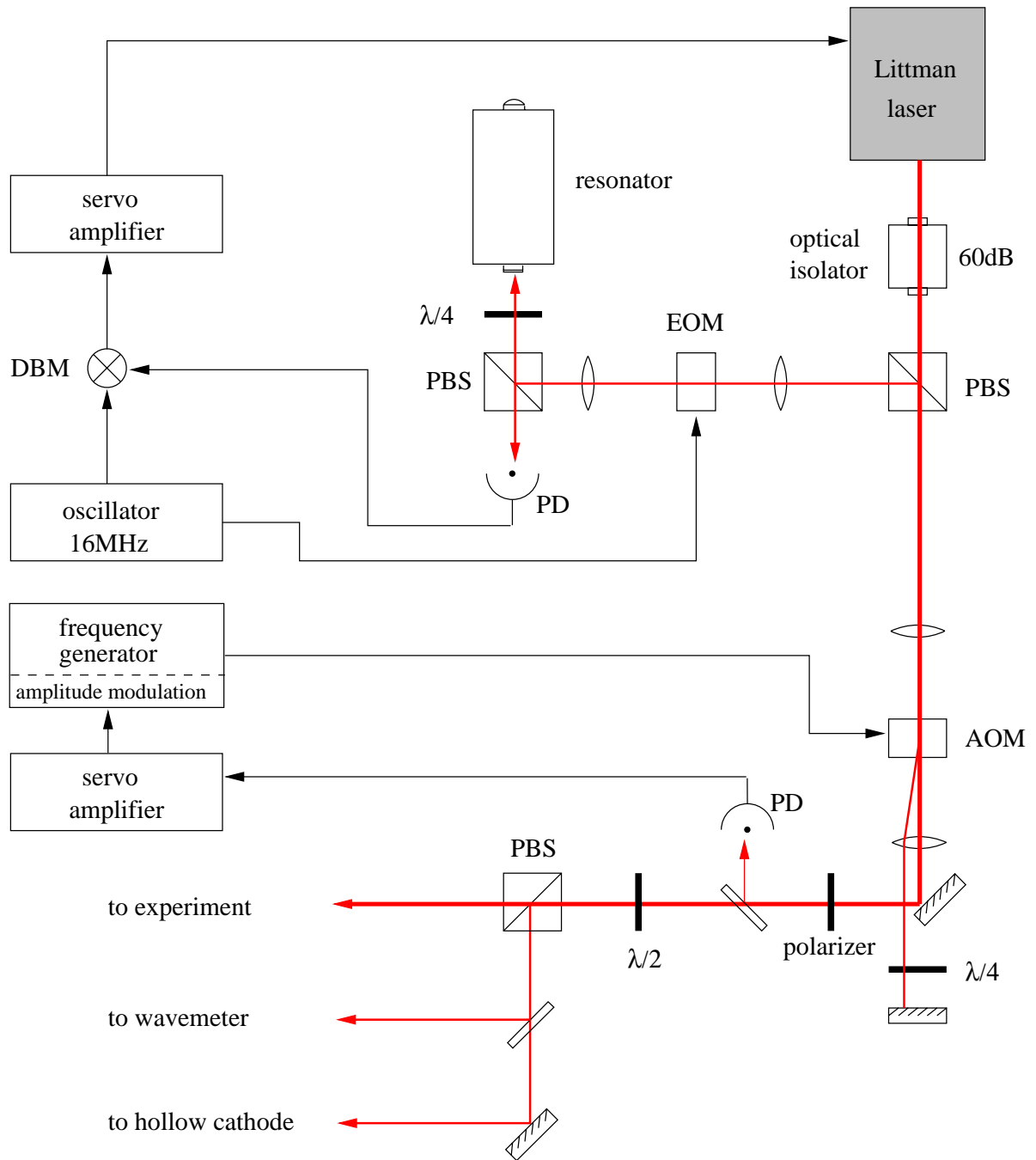
Figure 5.2: Setup of the red laser. The upper part shows the Pound-Drever locking scheme. In the lower part the AOM used for fine detuning and the intensity stabilisation is depicted. The first diffraction order is back reflected into the AOM and then used for the frequency stabilisation.

Measurements of the intensity fluctuations without the AOM amounted to 0.3% on the time scale from ns to μs and up to 1.5% on the timescale of 10s which would be sufficiently low. However, the diffraction efficiency of the acousto-optical effect depends on the frequency of the acoustic wave. At 200 MHz about 10% of the light intensity is diffracted into the first order. When the AOM is detuned ± 50 MHz this intensity dropped to almost zero and the frequency stabilization could not work. On the other hand the light intensity of the 0th order used for the experiment changed by more than 10% when the AOM was detuned. Additionally we observed that the polarization direction was turned by the AOM crystal each time the frequency or intensity of the acoustic wave was varied. Therefore an intensity stabilization was set up: A polarizer was introduced in the 0th order diffraction beam (see figure 5.2). The light intensity is then detected with a photo diode and the photo current is compared to a chosen level, to produce an error signal for the feeback circuit. The light intensity can be controlled by changing the intensity of the acoustic wave. This can be done by using the amplitude modulation facility of the frequency generator. The achieved laser detuning range, limited by the AOM efficiency, is 200 MHz. In this detuning range the light intensity fluctuations are below 1%. A power of 8 mW is available for the experiment. The laser linewidth is narrower than 100 kHz.
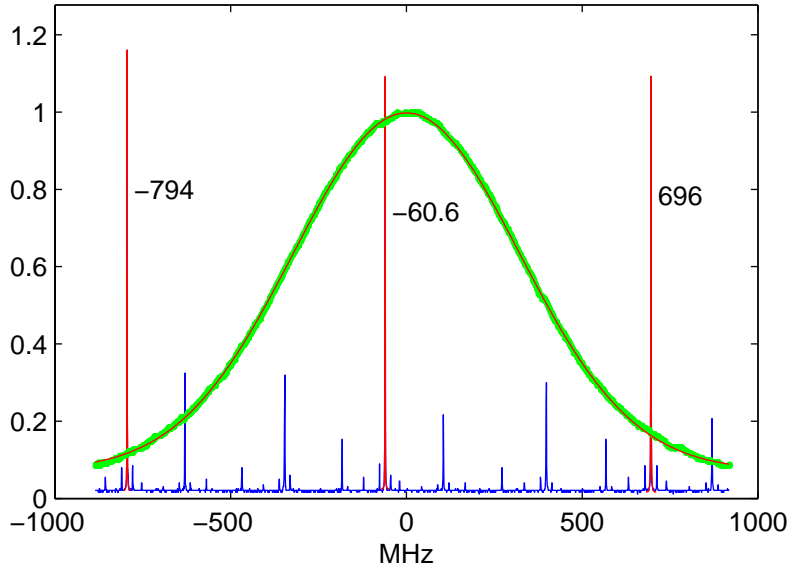
Figure 5.3: Hollow cathode spectrum at 650nm and transmission signal of the reference cavity. The cavity modes are not uniformely spaced due to laser drifts. $\text{FWHM}_{hollowcathode} \approx 750\text{MHz}$, Free spectral $\text{range}_{cavity}=745\text{MHz}$, Finesse$\approx 800$.

The cavity for the red laser has been built without a piezo in order to reduce cavity

drifts. Cavity resonances can be slowly tuned only by changing the temperature which is electronically stabilized. Fluctuations of temperature and atmospheric pressure still produce cavity drifts in the range of 100 MHz a day. It is possible to largely reduce drift rates, when the cavity is placed in a vacuum vessel and a second external temperature stabilization is built [40]. Ideally an atomic or molecular resonance is used as an absolute frequency reference (Te_2 at 493 nm [36], I_2 at 650 nm).

Two frequency references are used in the laboratory to find the Barium wavelengths: a wavemeter and a Barium hollow cathode lamp. The wavemeter determines the wavelength of a signal laser by comparing it to the wavelength of a monomode He-Ne-laser at 632 nm. Both lasers are coupled simultaneously and counterpropagating into a Michelson-interferometer. One of the interferometer arms consists of a corner cube reflector mounted on an air-cushion carriage. The number of interference fringes is counted and compared.

The optogalvanic spectroscopy with the Barium hollow cathode lamp is based on the effect that the current in a gas discharge changes with the population of the atomic energy levels of the involved atoms. When the hollow cathode is illuminated with resonant light the overall resistance changes. The weak electronic signal is measured with a lock-in technique. Figure 5.3 shows a hollow cathode spectrum at 650 nm and the transmission signal of the reference cavity.

Both lasers are spatially filtered to produce a gaussian beam shape of equal diameter. A half-wave plate and a polarizer serve to adjust the light intensities. The beams are combined using a dichroic mirror and focused in the trap center with an achromatic lens. The beam position can be optimized with two mirrors and the lens.

5.2   The vacuum vessel and the trap

The vacuum vessel with all its components is shown in figure 5.4.

The ion getter pump maintains a pressure of better than 10^{-8} mbar. The Barium oven produces an atomic beam. The atoms are ionized by an electron beam emitted by the electron gun opposite the Barium oven. The helical resonator on the top creates the high voltage of several 100 V at 18 MHz for the trap. The exact design of the trap electrodes is presented in figure 5.5.

Additional electrodes in the plane of the ring electrode allow one to compensate disturbing electric fields and to move the ion to the trap center where the micromotion can be prevented. Three coils produce the homogenous magnetic field perpendicular to the main beam direction.

Figure 5.4: The complete vacuum vessel.
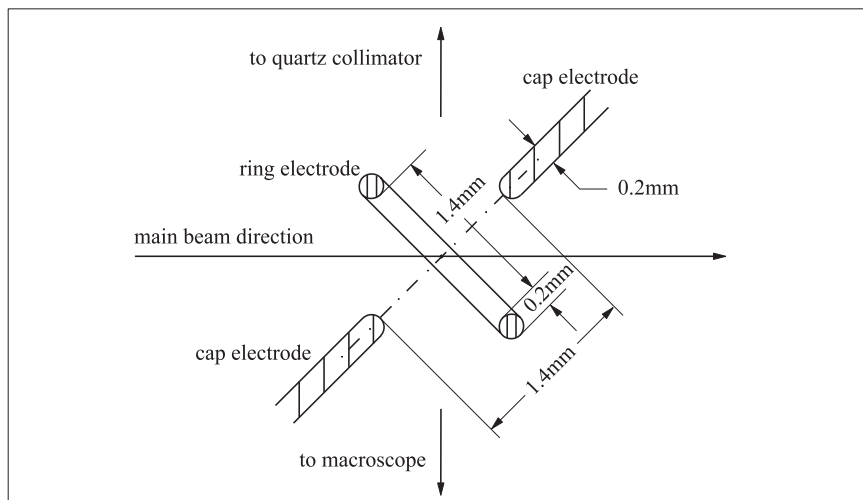
Figure 5.5: The trap electrodes in detail.

5.3   Fluorescence photon detection

The fluorescence light can be observed through two opposite CF100 flanges perpendicular to the main laser beam direction. The first detection channel consists of a light microscope with a fine adjustable objective. The ion can either be observed through a pair of oculars or is imaged onto a photomultiplier. For the second detection channel a quartz collimator has been placed inside the vacuum vessel in order to collect the fluorescent light within a larger solid angle. The ion is then imaged onto a second photomultiplier. Diaphragms are used to reduce straylight from the electrodes. Green filters assure that only green fluorescence photons strike the photomultiplier cathode. Both photomultipliers are cooled to $-30\,°C$ and have a dark counting rate of less than 6 cps. The quantum efficiency reaches approximately 26% at 493 nm. The photomultiplier pulses are amplified, discriminated and counted by a CAMAC system.

6 Measurements

6.1 Preparation of a single ion

All measurements start with the preparation of a single ion. For this purpose the lasers are set to the Barium wavelengths using the wavemeter and the Barium hollow cathode. The laser at 493 nm is tuned about 200-500 MHz below the atomic resonance for optical Doppler cooling on the $^2S_{1/2} \Leftrightarrow {}^2P_{1/2}$ transition. The Barium oven is heated to its working temperature and one tries to ionize an atom in the trap center with electron beam pulses. A produced ion is then immediately trapped and cooled. Since the human eye has its maximum sensitivity close to the 493 nm transition of Ba$^+$ it is possible to observe the fluorescence light emitted by one single ion directly with the eye, which facilitates the preparation of the ions. A small brilliant point can be seen in the trap center when the ion is well cooled and localized. Trapping of a single ion is also marked by a sudden jump in the photomultiplier counting rate. If more than one ion has been trapped several equally spaced jumps are observed and a small restless cloud appears. It is also possible to prepare crystals of up to four ions.

In order to assure that only one ion has been trapped, the light emitted by a Barium hollow cathode is focused into the trap. This light contains components at all possible Ba$^+$ transitions and allows one to excite the metastable $6^2D_{5/2}$ level. When this level is excited the fluorescence light suddenly disappears for a period corresponding to the lifetime of the state. This is a direct visualization of quantum jumps. The observed steps in the photon counting rate allow one to determine the number of trapped ions [41, 42].

6.2 Excitation spectra

An excitaton spectrum is the intensity of resonance fluorescence as a function of one of the laser detunings [43]. The intensity is measured by counting photons with pho-tomultipliers and does not contain any information about the spectral composition of the emitted light.
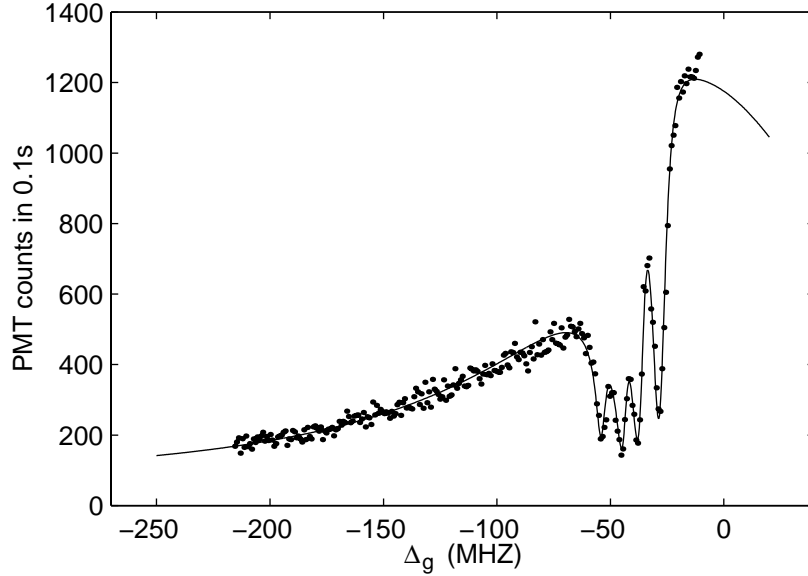
Figure 6.1: Scan of the laser at 493nm. Parameters: $S_g = 1.7 \pm 0.1$, $S_r = 2.6 \pm 0.2$, $\Delta_r = -41.4 \pm 0.5\,\mathrm{MHz}$, $u = 5.8 \pm 0.3\,\mathrm{MHz}$, $\alpha = 91 \pm 5°$, $\Gamma_l = 60 \pm 40\,\mathrm{kHz}$, dark counting rate ≈ 50.

Figure 6.1 shows a scan of the laser at $493\,\mathrm{nm}$ while the laser at $650\,\mathrm{nm}$ is kept at a fixed frequency below the D-P resonance. The laser is detuned by changing the resonance frequency of the reference resonator. The relative frequency axis was determined with the help of a Barium hollow cathode spectrum that had been simultaneously recorded. The power of the green laser was set to $25\,\mu\mathrm{W}$ and that of the red laser to $9\,\mu\mathrm{W}$. An angle of $90°$ was chosen between polarization and magnetic field. As predicted by the model four dark resonances appear at $\Delta_r = \Delta_g \pm \frac{3}{5}u$, $\pm\frac{11}{5}u$. In order to assure permanent Doppler cooling the laser should be kept below the $\mathrm{Ba^+}$ resonances. When the lasers are tuned too far above resonance the ion heats up and the fluorescence intensity drops.

The solid line in figure 6.1 is a fit to the data calculated with the eight level Bloch equations described in chapter 3. The fit allows one to determine the experimental parameters. In addition to the parameters discussed in 3.3 the zero point of the frequency axis and a constant background counting rate are considered.

The laser linewidths are not calculated separately but it is assumed that both lasers have the same linewidth $\Gamma_{lg} = \Gamma_{lr} = \Gamma_l/2$. It should be noted that the laser linewidths are fit parameters that can be determined only with a relatively high uncertainty from the excitation spectra. In principle the green laser would broaden the whole spectrum but this effect is negligible considering that the laser linewidth is more than three

orders of magnitude narrower than the spectrum. The spectrum is essentially power broadened. On the other hand both lasers contribute in equal shares to the reduced depth of the dark resonances. Hence it is impossible to distinguish the effects of the red and the green laser on the spectra.
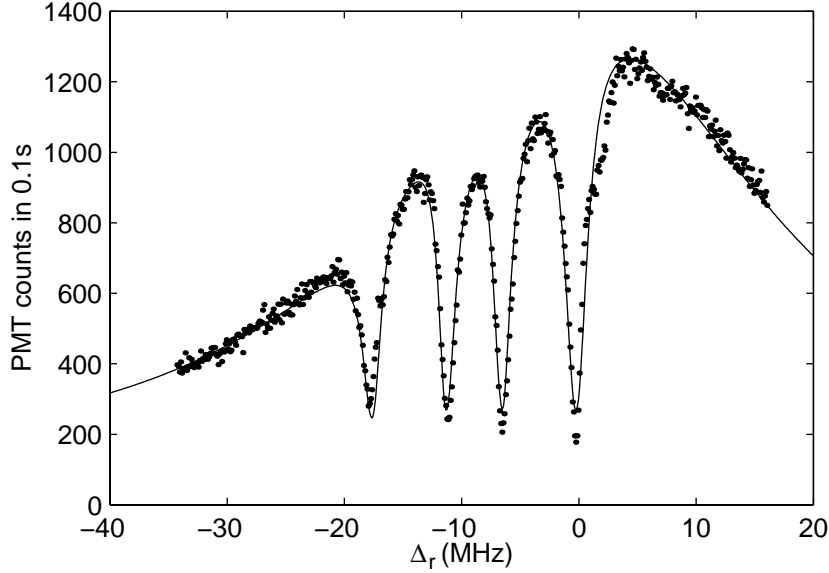
Figure 6.2: Scan of the laser at 650nm. Parameters: $S_g = 0.42 \pm 0.05$, $S_r = 1.25 \pm 0.06$, $\Delta_g = -8.9 \pm 0.2\,\text{MHz}$, $u = 3.95 \pm 0.1\,\text{MHz}$, $\alpha = 90 \pm 3°$, $\Gamma_l = 60 \pm 25\,\text{kHz}$, dark counting rate ≈ 70.

Figure 6.3 and 6.2 are scans of the red laser over the atomic resonance with the green laser kept at a fixed frequency. The red laser was detuned in $100\,\text{kHz}$ steps using a frequency generator and the double pass AOM. Both spectra show narrow dark resonances. One of them, with a width of $\approx 1\,\text{MHz}$, is plotted in figure 6.4.

The spectrum in figure 6.5 shows four dark resonances at $\Delta_r = \Delta_g \pm \frac{7}{5}u$, $\pm \frac{11}{5}u$ corresponding to an angle of $\alpha = 65°$ between polarization and magnetic field. This configuration was achieved by switching of the coils used to compensate the earth magnetic field.

It may seem strange that the dark resonances at $\Delta_r = \Delta_g \pm \frac{3}{5}u$ are almost completely suppressed although all Zeeman transitions are excited at this angle. The dark resonaces at $\Delta_r = \Delta_g + \frac{3}{5}u$ correspond to superpositions of the states $6S_{1/2}$ $m_j = +1/2$ and $5D_{3/2}$ $m_j = +1/2$. This superposition is generated via the interaction with the Zeeman sublevels of the $6P_{1/2}$ state. Since there are two of these states there are two ways to excite the dark resonances (see figure 6.6). At a certain angle the two ways of excitation cancel each other out. In figure 6.7 the coherence $\rho_{27} = |\rho_{27}|e^{i\,\text{phase}}$, which
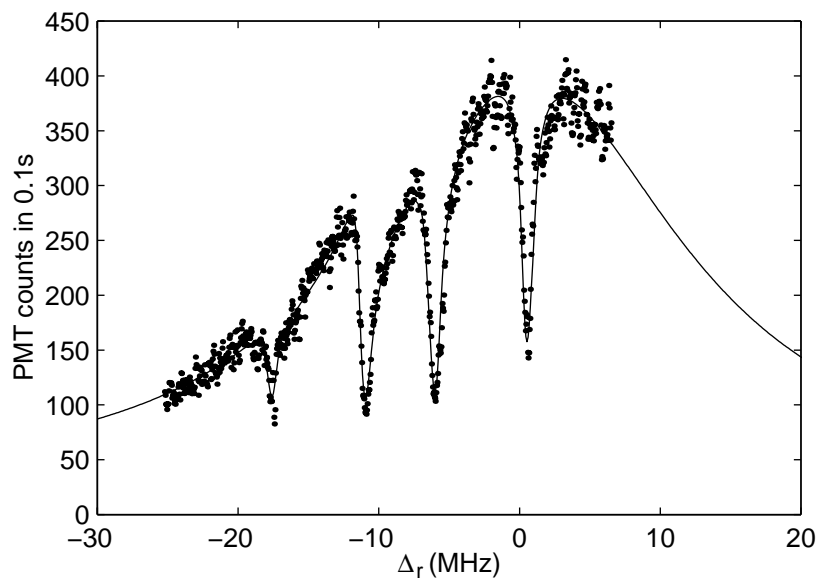
Figure 6.3: Scan of the laser at 650nm. Parameters: $S_g = 0.33$, $S_r = 0.52$, $\Delta_g = -8.55\,\text{MHz}$, $u = 4.1\,\text{MHz}$, $\alpha = 90°$, $\Gamma_l = 60\,\text{kHz}$, dark counting rate ≈ 20
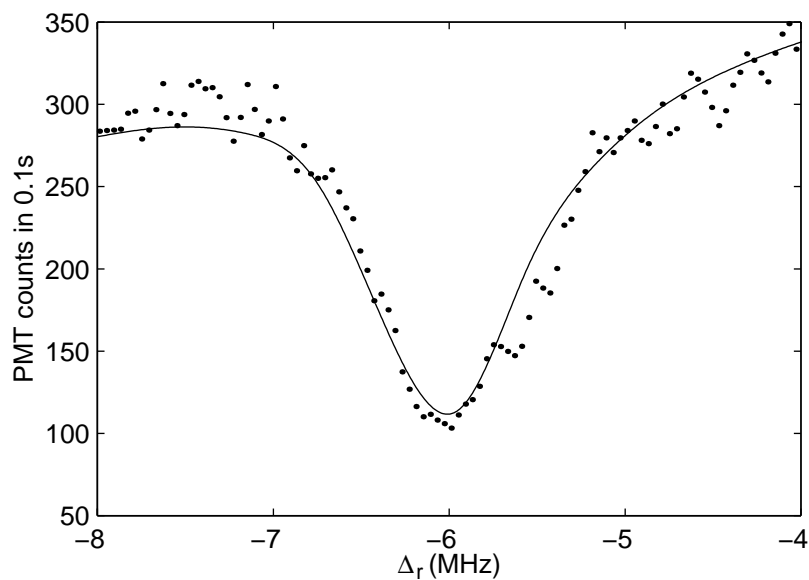
Figure 6.4: One of the dark resonances of figure 6.3 in detail.

describes the dark resonances at $\Delta_r = \Delta_g + \frac{3}{5}u$, is plotted as a function of α. $|\rho_{27}|$ has its minimum at $\alpha = 56.6°$.
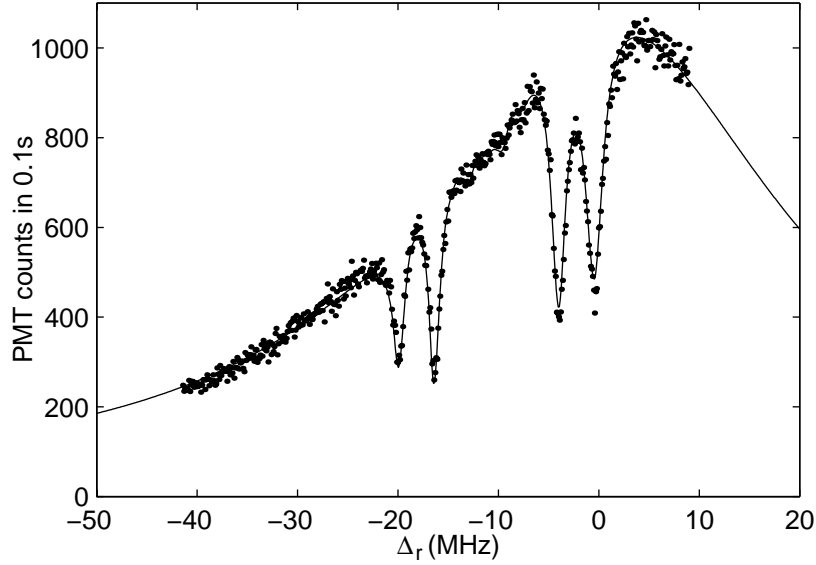
Figure 6.5: Scan of the laser at 650nm. Parameters: $S_g = 0.39 \pm 0.05$, $S_r = 1.14 \pm 0.06$, $\Delta_g = -10.1 \pm 0.2\,\text{MHz}$, $u = 4.41 \pm 0.2\,\text{MHz}$, $\alpha = 65 \pm 3°$, $\Gamma_l = 10 \pm 10\,\text{kHz}$, dark counting rate ≈ 20.
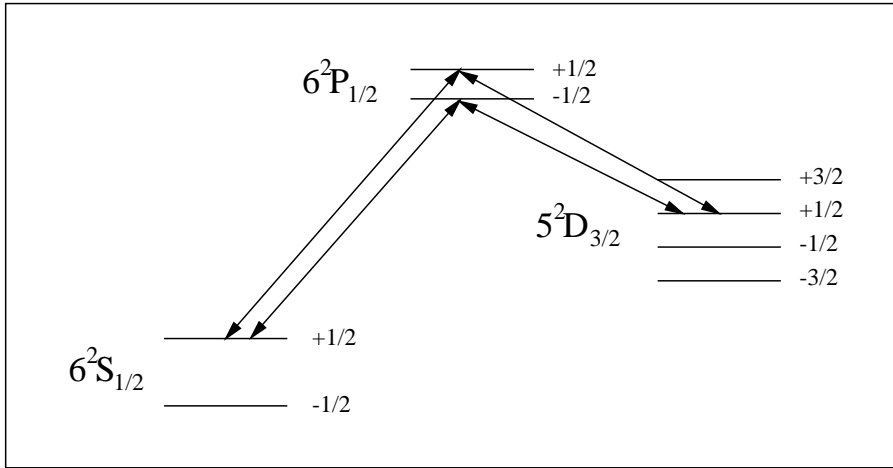
Figure 6.6: The two excitation channels for the dark resonance at $\Delta_r = \Delta_g + 3/5u$.

The scan of the red laser in figure 6.8 was recorded with high micromotion amplitude. Sidebands of the dark resonances appear which can be well reproduced by the model described in chapter 4. The fit was first calculated without the modulation. The result then served as initial condition for a second fit. A velocity amplitude of $3.7 \pm 0.7\,\text{m/s}$ and a trap drive frequency of 21 ± 3 MHz are found as fitting parameters. This corresponds
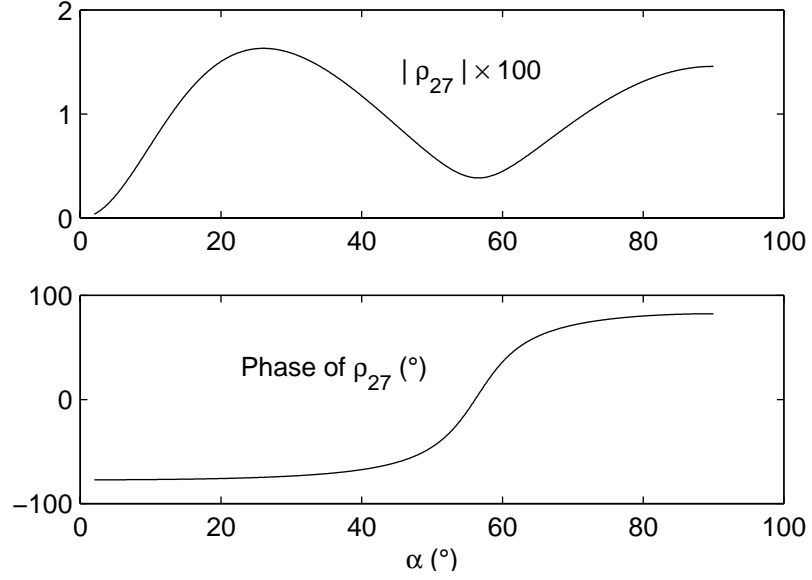
Figure 6.7: The coherence ρ_{27} versus the angle α between polarization and magnetic field plotted at $\Delta_r = \Delta_g + \frac{3}{5}u$. At an angle of $57°$ the coherence is very small and the corresponding dark resonance cannot be observed. Parameters: $S_g = 0.39$, $S_r = 1.14$, $\Gamma_l = 0$, $u/2\pi = 4.41\,\mathrm{MHz}$, $\Delta_g/2\pi = -10.1\,\mathrm{MHz}$, $\Delta_r = \Delta_g + \frac{3}{5}u$.

to a kinetic energy of

$$E_{kin} = \frac{m}{2}\langle(v_0\cos(\Omega\,t))^2\rangle = \frac{m}{4}v_0^2 = (4.9 \pm 1.9) \times 10^{-6}\,eV \tag{6.1}$$

and to an oscillation amplitude of $v_0/\Omega = 0.18 \pm 0.04\,\mu\mathrm{m}$.
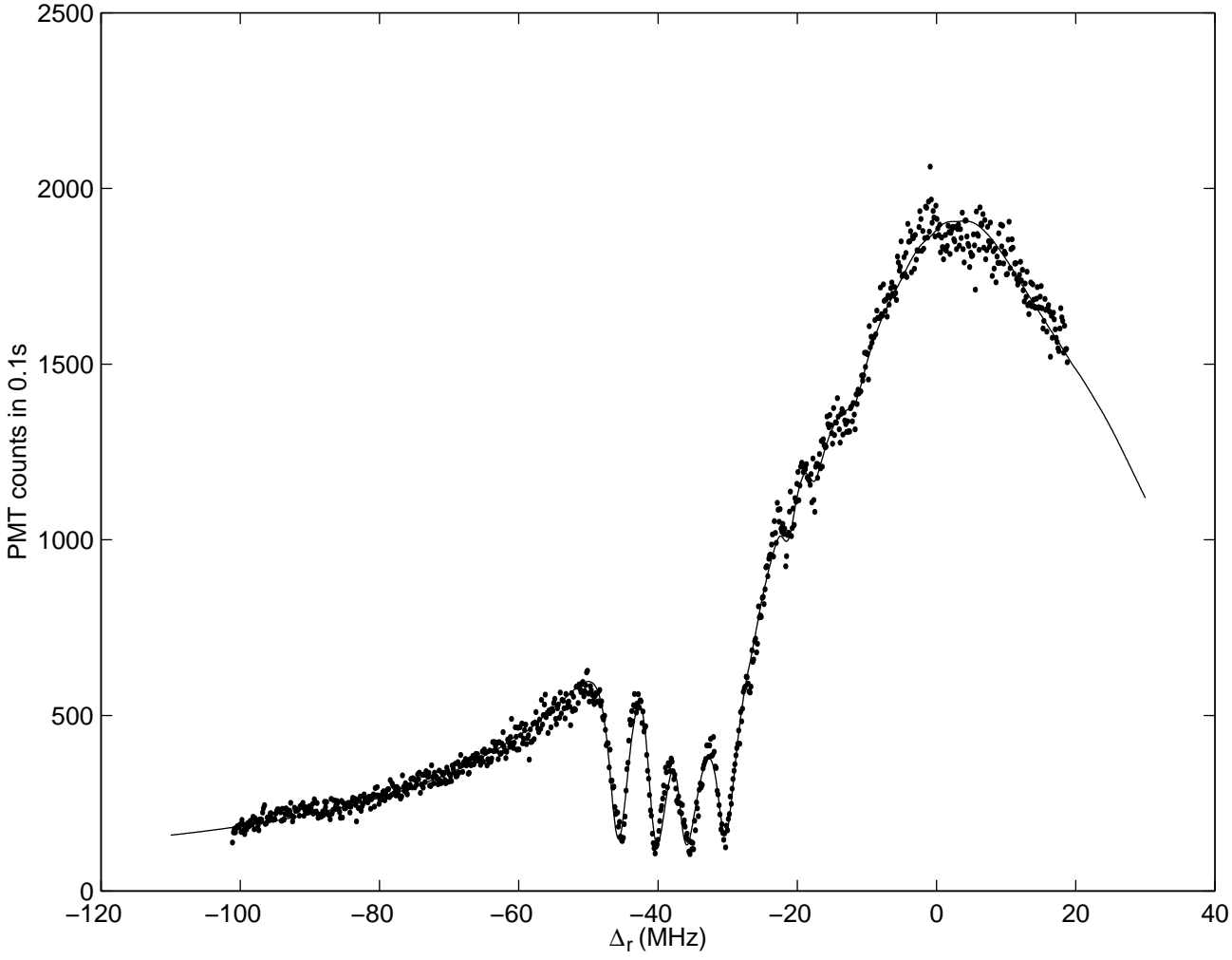
Figure 6.8: Scan of the laser at 650nm with micromotion sidebands of the four dark resonances. Parameters: $S_g = 1.22 \pm 0.05$, $S_r = 2.18 \pm 0.1$, $\Delta_g = -38 \pm 0.4\,\text{MHz}$, $u = 3.47 \pm 0.2\,\text{MHz}$, $\alpha = 92 \pm 3°$, $\Gamma_l = 20 \pm 20\,\text{kHz}$, dark counting rate $= 40 \pm 20$, $\Omega = 21 \pm 3\,\text{MHz}$, $v_0 = 3.7 \pm 0.7\,\text{m/s}$.

6.3   Analysis of the ion motion

When the ion is stored it is interesting to analyse its motion in the trap, particularly the frequency components of its oscillation.

Frequencies in the acoustic region of a few hundred Hz may be produced by badly earthed components around the trap. In fact we have observed that the ion oscillates at 100 Hz when the coils used to produce the magnetic field were not connected to the trap ground. In the macroscope a straight line appeared instead of a well localized point. First of course it has not been clear which component caused this effect and at which frequency. An acousto-optical modulator was introduced in the green laser beam for periodically switching the laser on and off. When the AOM was operated with pulses at approximately 100 Hz a kind of beat between the oscillation of the ion in the trap and the chopped laser could be seen. The stroboscopic illumination enabled us to resolve the details of the motion.

The secular frequencies are found in the range of 200 kHz to 2 MHz. They depend on the power applied to the helical resonator and can be measured by applying an additional small AC-voltage to the cap electrodes. When this AC-voltage is resonant with one of the secular frequencies the oscillation amplitude increases which leads to a drop in the fluorescence light intensity. Under standard working conditions the secular frequencies along the x,y and z-axes are approximately 630 kHz, 680 kHz and 1.2 MHz, respectively.

Another efficient and widely used tool to study the dynamics of particles stored in traps are correlation measurements. They are suited to analyse the internal dynamics, i.e. the population of atomic energy levels, as well as the external dynamics, i.e. the movement of the particles in the trap.

The second order correlation function $g^{(2)}(\tau)$ is proportional to the probability of detecting a photon at time t+τ given that a photon had been detected at time t. For a single ion this function tends towards zero for small values of τ which reflects the fact that the ion cannot emit two photons simultaneously. After emission of a photon the ion is in one of its ground states and must be reexcited before it can emit another photon. This effect is called anti-bunching. It can be shown that $g^{(2)}(\tau)$ is proportional to the time evolution of the excited states with an initial condition depending on the properties, i.e. the wavelength and polarisation, of the first detected photon. Correlation measurements directly reveal the atomic dynamics. As we have seen in chapter 4 the fluorescence light emitted by a stored ion is modulated due to the first order Doppler effect when the ion oscillates in the trap. This causes a modulation of the correlation function. In principle all frequency components of the oscillation can be studied with this method as far as their oscillation amplitude exceeds the laser wavelength.

Two types of correlation measurements have been performed with our experimental setup. The first is the correlation between the driving AC trap voltage and the detected

photons. Since the phases of the micromotion and the driving potential are rigidly coupled this measurement allows one to determine the micromotion amplitude. A time-to-digital-converter(TDC) is used to measure the time delays between a detected photon and a fixed phase of the AC-potential, whereby the detected photon serves as start pulse and the AC-phase as stop pulse. The time delays are stored in a histogram unit. A histogram obtained in this way is shown in figure 6.9.
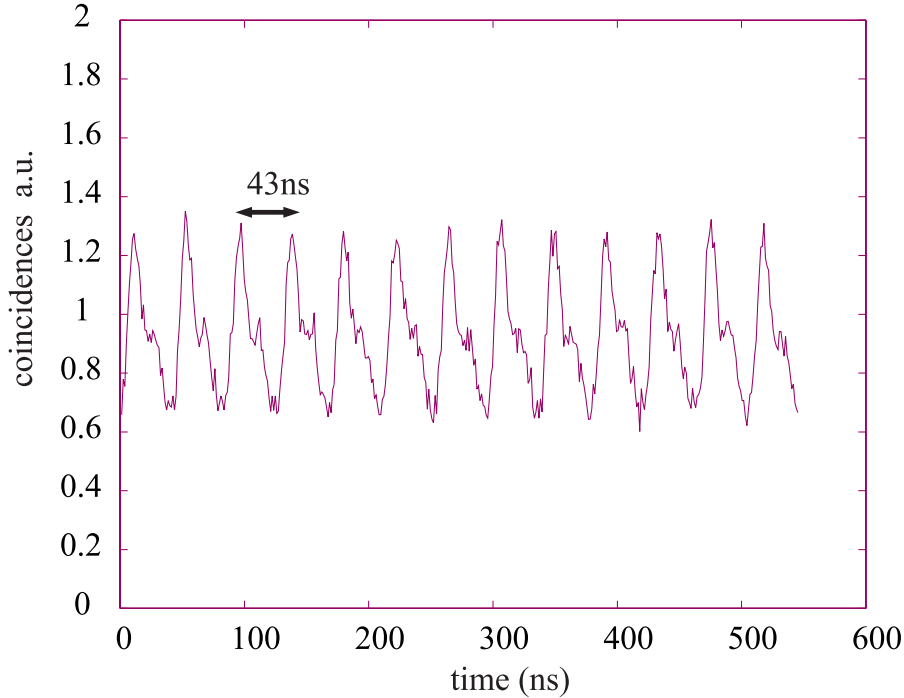
Figure 6.9: Measurement of the correlation between the AC trap potential and the detected photons. The 43 ns period corresponds to the 23.4 MHz trap frequency.

The modulation at the trap frequency is clearly visible. The amplitude of this modulation depends on the micromotion amplitude, the laser detunings and on the laser beam direction. Since the micromotion amplitude is proportional to the distance of the ion to the trap center (eqn.(4.10)) a strong modulation indicates that the ion has been shifted out of the trap center by disturbing potentials around the trap. These potentials may be produced for example by electrons from the electron gun that accumulate on the quartz collimator inside the vacuum vessel. By applying a voltage to the cap electrodes and to the auxiliary electrodes in the ring plane it is possible to compensate the disturbing potentials in all directions and hence to push the ion in the trap center. Of course, the modulation contains information only about the micromotion component

parallel to the laser beam. For perfectly compensating the micromotion it is therefore necessary to illuminate the ion with lasers from three independent directions.

A good micromotion compensation is indispensible for precision spectroscopy. On the other hand the micromotion is well suited to study the effects of any oscillations of a stored particle on the resonance fluorescence, as sidebands in the spectrum of resonance fluorescence or sidebands to the dark resonances in excitation spectra.

The second type of correlation function that has been measured is the photon-photon correlation $g^{(2)}(\tau)$. For this purpose both photomultipliers are used: The TDC is started by pulses from the first photomultiplier and stopped by pulses from the second. An artificial delay in the stop line translates the time origin of the created histogram.
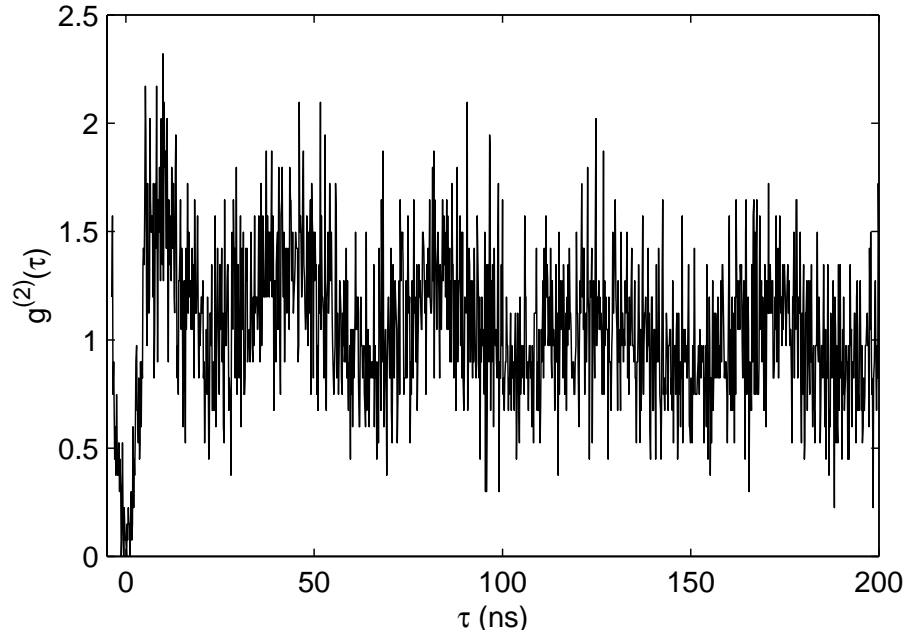
Figure 6.10: Measurement of the second order correlation function showing antibunching and micromotion modulation. Time resolution: 156 ps. Time overflow: 400 ns.

Figure 6.10 shows a measurement of the photon-photon correlation. It can be seen that $g^{(2)}(\tau)$ vanishes for $\tau = 0$ which proves the antibunching property of the single ion resonance fluorescence. The details of the internal atomic dynamics are however hidden by a strong micromotion modulation. At longer time delays the secular motion could be visualized as well.

When the micromotion is compensated and the secular motion damped by laser cooling the atomic dynamic appears in the histogram [25, 44]. The dynamic can be perfectly

described by the model discussed in chapter 3. Green filters have been introduced in both detection channels. Hence, the measured correlation function describes the conditional probability of detecting a green photon perpendicular to the laser beam direction at time t+τ when such a photon has been detected at time t. It can be shown [25] that under these conditions

$$g^{(2)}(\tau) = \frac{\rho_{33}(\tau) + \rho_{44}(\tau)}{\rho_{33}(\infty) + \rho_{44}(\infty)} \tag{6.2}$$

with the initial condition:

$$\rho_{11}(0) = \frac{\rho_{44}(\infty)}{\rho_{33}(\infty) + \rho_{44}(\infty)} \tag{6.3}$$

$$\rho_{22}(0) = \frac{\rho_{33}(\infty)}{\rho_{33}(\infty) + \rho_{44}(\infty)}. \tag{6.4}$$

The initial state represents a mixed state, reflecting the fact that the population of the excited Zeeman sublevels $|3\rangle$ and $|4\rangle$ is projected on the Zeeman sublevels of the ground state, when the first photon is emitted. These photons are always circularly polarized corresponding to $\Delta m_j = \pm 1$ transitions. Since start and stop photons have the same properties (there are green filters in front of both photomultipliers) the correlation function is the same for negative and positive time delays: $g^{(2)}(-t) = g^{(2)}(t)$. Imagine, however, that a red filter is introduced in front of one of the photomultipliers. Then the measured correlation function is different for positive and negative delays: On the positive branch it describes the probability of detecting a photon at $t + \tau$ given that a red photon has been detected at time t. The negative branch is the same as before.

Figure 6.11 shows a measurement of the photon correlation with the micromotion compensated. The theoretical curve was calculated with the parameters determined from the corresponding excitation spectrum plotted in figure 6.12. Three parameters had to be fitted: The detuning of the laser at 650nm, an additional offset and the mutiplicative factor.
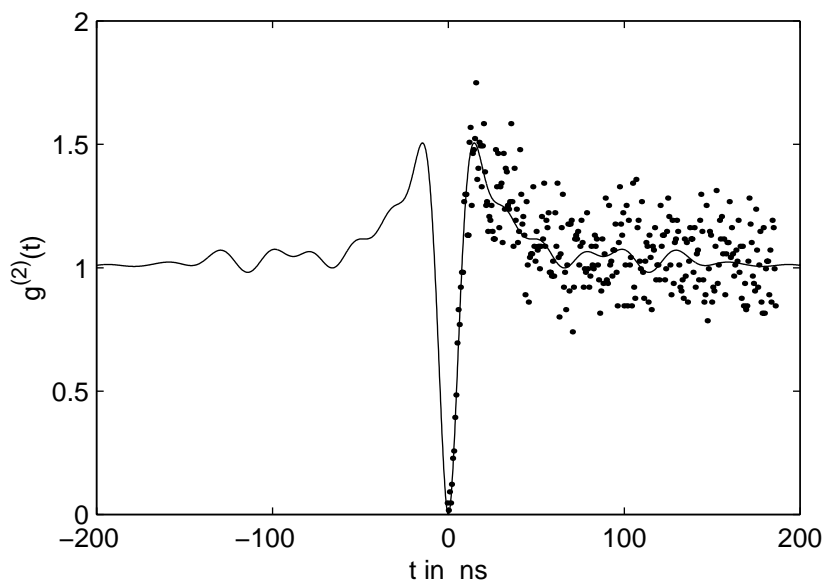
Figure 6.11: Measurement of the photon correlation $g^{(2)}(t)$. Parameters determined from excitation spectrum in figure 6.12. The red laser detuning and the normalization factor had to be fitted: $\Delta_r = 7 \pm 12 \, \text{MHz}$. The data have been divided by the determined normalization factor.
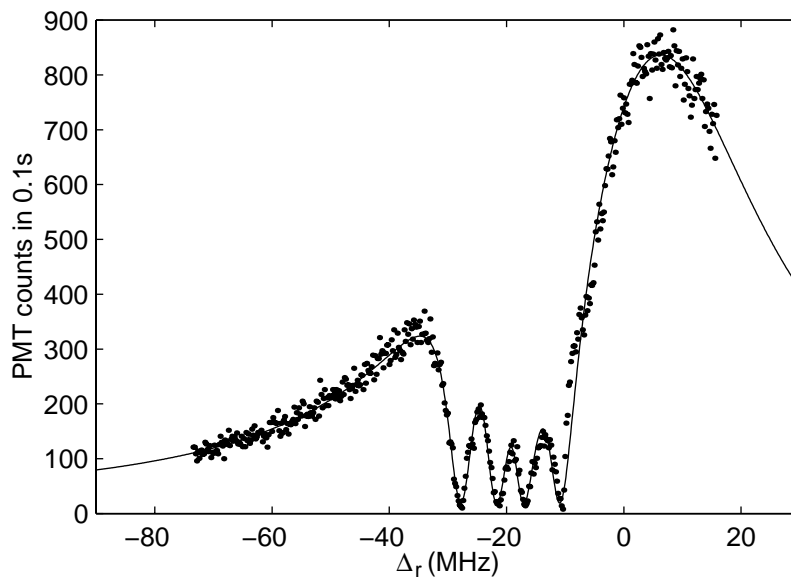
Figure 6.12: Scan of the laser at 650nm. Parameters used in figure 6.11: $S_g = 1.2 \pm 0.1$, $S_r = 2.6 \pm 0.2$, $\Delta_g = -19.4 \pm 0.3 \, \text{MHz}$, $u = 3.8 \pm 0.2 \, \text{MHz}$, $\alpha = 90 \pm 3°$, $\Gamma_l = 7 \pm 7 \, \text{kHz}$, dark counting rate $= 14 \pm 10$.

7 Summary and outlook

This thesis introduces some basic tools to analyse the fluorescence light emitted by a single Ba^+ ion, which is confined in a Paul trap and illuminated with two laser light sources.

Three fine structure levels of Ba^+, the $6^2S_{1/2}$, $6^2P_{1/2}$ and $5^2D_{5/2}$ levels, are coupled via the interaction with two laser light fields at 493 nm and 650 nm. In an external magnetic field, which defines the quantization axis, the three levels split up into eight Zeeman sublevels.

The eight level Bloch equations, which perfectly reproduce the measured experimental data, can be derived from the quantum mechanical model of the light-matter interaction. In this model the atomic system, the light fields and their interaction are described with quantum mechanical operators. The spontaneous decay of excited states is introduced using the density matrix formalism.

When the detunings of the two lasers with respect to the atomic transition frequencies are equal, the ion is optically pumped into a coherent superposition of the two ground states. This effect is called dark resonance because the ion does not scatter light in this state.

Another pure quantum effect can be observed in photon correlation measurements. The probability of detecting two photons within a short time delay is very small. After emission of a first photon the atom is in its ground state and must be reexcited before the emission of a second photon.

The ion is confined in a Paul trap. Two frequency components can be distinguished in its motion: The micromotion is driven by the applied rf potential and can be minimized by compensating disturbing electrostatic stray fields. The secular motion at lower frequencies corresponds to the motion of a harmonic oscillator and is damped with laser cooling on the S-P transition.

The oscillation of the confined ion leads to a modulation of the fluorescent light due to the Doppler effect. This modulation appears in the photon correlation and produces motional sidebands of the dark resonances.

Two diode lasers in Littman-Metcalf configuration generate light at 650 nm and 986 nm, which is frequency doubled. Their linewidths are reduced by electronic stabilization

using the Pound-Drever locking scheme. The laser at 650 nm is fine detuned with an acousto optical modulator: for this purpose a light intensity stabilization was built.

Several tools are available to study the ion motion: stroboscopic illumination at acoustic frequencies, the correlation between the driving trap potential and the detected photons to analyse the micromotion, and the photon-photon correlation.

Excitation spectra of a Ba^+ ion, i.e. the fluorescence rate vs. the laser detuning, were recorded with different experimental parameters. The fit to the data with the eight level Bloch equations allows one to determine the experimental parameters. The dependence of the dark resonances on the laser intensities and on the orientation of the magnetic field and the light polarization was studied. Also the effect of a large micromotion amplitude on the spectra agrees well with the calculations.

In future some changes of the laser setup are envisaged: in order to improve the long-term stability it is planned to use the molecular resonances of Te_2 at 493 nm as an absolute frequency reference. The Te_2 resonances have already been investigated using modulation transfer spectroscopy [36]. One of the Te_2 lines has a distance of only 330 MHz to the Barium resonance. The laser at 493 nm would then be detuned with an acousto-optical modulator as well. The laser at 650 nm could be stabilized to a resonance of I_2. Saturation spectroscopy on these weak I_2 lines, however, requires almost all of the available laser intensity. The better solution will be to build up a new more stable reference cavity. For this purpose the cavity should be placed in a temperature stablized and air-tight box. Additionally, a second external temperature stabilization should be built.

While this thesis was written, the next important problem was tackled by Christoph Raab: the measurement of the spectrum of resonance fluorescence. This spectrum can be calculated using the eight level Bloch equations [25] and contains an inelastic and an elastic scattering contribution. In addition when the ion oscillates in the trap, sidebands of the elastic scattering peak appear at the micromotion and secular frequencies [45]. A heterodyne measurement scheme is used to study these sidebands. The micromotion sidebands have already been observed. The next step will be to further improve the signal-to-noise ratio in order to resolve also the broader sidebands at the secular frequencies. This will allow an investigation of the laser cooling process.

8 Appendix

8.1 Transformation of the Hamiltonian

When a quantum mechanical state $|\Psi\rangle$ is transformed with the Operator U

$$|\Psi'\rangle = U\,|\Psi\rangle \qquad UU^\dagger = U^\dagger U = 1$$

then the corresponding transformation for the Hamiltonian $\hat{\mathcal{H}}$ can be calculated as follows:

$$
\begin{aligned}
i\hbar\frac{d}{dt}|\Psi'\rangle &= i\hbar\frac{d}{dt}\left(U\,|\Psi\rangle\right) = i\hbar UU^\dagger\frac{d}{dt}\left(U\,|\Psi\rangle\right) \\
&= i\hbar U\left(\frac{d}{dt}\left(U^\dagger U\,|\Psi\rangle\right) - \frac{dU^\dagger}{dt}U\,|\Psi\rangle\right) \\
&= U\left(\hat{\mathcal{H}}U^\dagger U\,|\Psi\rangle - i\hbar\frac{dU^\dagger}{dt}U\,|\Psi\rangle\right) \\
&= \underbrace{\left(U\hat{\mathcal{H}}U^\dagger - i\hbar U\frac{dU^\dagger}{dt}\right)}_{\hat{\mathcal{H}}'} U\,|\Psi\rangle
\end{aligned}
$$

We have used:

$$i\hbar\frac{d}{dt}|\Psi\rangle = \hat{\mathcal{H}}\,|\Psi\rangle$$

The calculation can also be made using the density operator formalism which yields the same result.

8 Appendix

8.2 Matrix elements of the dipole operator

In order to calculate the matrix elements of the interaction Hamiltonian for the atomic system with eight Zeeman sublevels in chapter 3 it is necessary to determine the matrix elements of the dipole operator $\vec{D}_{ab} = \langle a|\vec{D}|b\rangle$. The result of this calculation is summarized here:

$$\vec{D}_{31} = d_g \begin{pmatrix} 0 \\ 0 \\ \frac{1}{\sqrt{3}} \end{pmatrix} \qquad \vec{D}_{41} = d_g \begin{pmatrix} -\frac{1}{\sqrt{3}} \\ i\frac{1}{\sqrt{3}} \\ 0 \end{pmatrix}$$

$$\vec{D}_{32} = d_g \begin{pmatrix} -\frac{1}{\sqrt{3}} \\ -i\frac{1}{\sqrt{3}} \\ 0 \end{pmatrix} \qquad \vec{D}_{42} = d_g \begin{pmatrix} 0 \\ 0 \\ -\frac{1}{\sqrt{3}} \end{pmatrix}$$

$$\vec{D}_{35} = d_r \begin{pmatrix} -\frac{1}{2} \\ i\frac{1}{2} \\ 0 \end{pmatrix} \qquad \vec{D}_{45} = 0$$

$$\vec{D}_{36} = d_r \begin{pmatrix} 0 \\ 0 \\ -\frac{1}{\sqrt{3}} \end{pmatrix} \qquad \vec{D}_{46} = d_r \begin{pmatrix} -\frac{1}{2\sqrt{3}} \\ i\frac{1}{2\sqrt{3}} \\ 0 \end{pmatrix}$$

$$\vec{D}_{37} = d_r \begin{pmatrix} \frac{1}{2\sqrt{3}} \\ i\frac{1}{2\sqrt{3}} \\ 0 \end{pmatrix} \qquad \vec{D}_{47} = d_r \begin{pmatrix} 0 \\ 0 \\ -\frac{1}{\sqrt{3}} \end{pmatrix}$$

$$\vec{D}_{38} = 0 \qquad \vec{D}_{48} = d_r \begin{pmatrix} \frac{1}{2} \\ i\frac{1}{2} \\ 0 \end{pmatrix}$$

8.3 Computer programs

This section shows the detailed procedure to calculate the optical Bloch equations with a computer program and the MATLAB programs used in this paper to calculate the theoretical curves. The computer programs are based on programs from Jürgen Eschner.

Starting point is the Liouville equation for the $N \times N$ density matrix ρ:

$$\frac{d\rho}{dt} = -\frac{i}{\hbar}\left(\mathcal{H}\rho - \rho\mathcal{H}\right) - \frac{1}{2}\sum_m \left(\hat{C}_m^\dagger \hat{C}_m \rho + \rho \hat{C}_m^\dagger \hat{C}_m - 2\hat{C}_m \rho \hat{C}_m^\dagger\right)$$

which can also be written differently:

$$\frac{d\rho}{dt} = -\frac{i}{\hbar}\left(\left(\mathcal{H} - \frac{i\hbar}{2}\sum_m \hat{C}_m^\dagger \hat{C}_m\right)\rho - \rho\left(\mathcal{H} + \frac{i\hbar}{2}\sum_m \hat{C}_m^\dagger \hat{C}_m\right)\right) + \sum_m \hat{C}_m \rho \hat{C}_m^\dagger$$

$$= -\frac{i}{\hbar}\left(\tilde{\mathcal{H}}\rho - \rho\tilde{\mathcal{H}}^\dagger\right) + \sum_m \hat{C}_m \rho \hat{C}_m^\dagger$$

where we have introduced the effective Hamiltonian $\tilde{\mathcal{H}}$.

$$\tilde{\mathcal{H}} = \mathcal{H} - \frac{i}{2\hbar}\sum_m \hat{C}_m^\dagger \hat{C}_m$$

Note that $\tilde{\mathcal{H}}$ is no longer hermitian. The terms $\sum_m \hat{C}_m \rho \hat{C}_m^\dagger$ are often called 'feeding' terms: They have to be added in order to fulfil the normalization condition $\sum_n \rho_{nn} = 1$. The population of a decaying excited state must reappear in the ground states.

Since the Liouville equation is linear in the components of ρ it can be written in the following form:

$$\frac{d\rho_{rs}}{dt} = -\frac{i}{\hbar}\langle r|\left(\tilde{\mathcal{H}}\rho - \rho\tilde{\mathcal{H}}^\dagger\right)|s\rangle + \langle r|\sum_m \hat{C}_m \rho \hat{C}_m^\dagger|s\rangle$$

$$= -\frac{i}{\hbar}\left(\sum_k \tilde{\mathcal{H}}_{rk}\rho_{ks} - \sum_j \rho_{rj}\tilde{\mathcal{H}}_{js}^\dagger\right) + \sum_m \sum_{kj} \langle r|C_m|k\rangle\langle k|\rho|j\rangle\langle j|C_m^\dagger|s\rangle$$

$$= -\frac{i}{\hbar}\left(\sum_{kj} \tilde{\mathcal{H}}_{rk}\delta_{js}\,\rho_{kj} - \sum_{kj} \tilde{\mathcal{H}}_{js}^\dagger\delta_{rk}\,\rho_{kj}\right) + \sum_{kj}\sum_m (C_m)_{rk}(C_m^\dagger)_{js}\,\rho_{kj}$$

$$= \sum_{kj}\left(-\frac{i}{\hbar}\left(\tilde{\mathcal{H}}_{rk}\delta_{js} - \tilde{\mathcal{H}}_{js}^\dagger\delta_{rk}\right) + \sum_m (C_m)_{rk}(C_m^\dagger)_{js}\right)\rho_{kj}$$

8 Appendix

Hence:

$$\frac{d\rho_{rs}}{dt} = \sum_{kj} L_{rs,kj}\,\rho_{kj}$$

with

$$L_{rs,kj} = -\frac{i}{\hbar}\left(\tilde{\mathcal{H}}_{rk}\delta_{js} - \tilde{\mathcal{H}}^{\dagger}_{js}\delta_{rk}\right) + \sum_{m}(C_m)_{rk}(C_m^{\dagger})_{js}.$$

The $N^2 \times N^2$ matrix L is called Liouville matrix.

```
function L=b311(O12,O23,D1,D2,l1,l2)


% Program to calculate the Liouville matrix L
% for a three level system in lambda-configuration.
%  O12, O23 ... Rabi frequencies in MHz
%  D1, D2   ... Detunings in MHz


gg=15.1;         % Decay constants for Ba ions in  MHz
gr=5.3;


l1=l1/1000;     % Laser linewidths are given in kHz
l2=l2/1000;


z=3;
E=eye(z);
ii=(1:z)'*ones(1,z);
i1=reshape(ii',1,z^2);     % first index
i2=reshape(ii, 1,z^2);     % second index


% Coherent hamiltonian
H=[D1 -O12/2 0 ; -O12/2 0 -O23/2 ; 0 -O23/2 D2];


% Relaxation
C1=gg^0.5*E(:,1)*E(2,:);
C2=gr^0.5*E(:,3)*E(2,:);


C3=(2*l1)^0.5*E(:,1)*E(1,:);
C4=(2*l2)^0.5*E(:,3)*E(3,:);


CC=C1'*C1+C2'*C2+C3'*C3+C4'*C4;


% Effective Hamiltonian
H=H-i/2*CC;
Hc=H'.';


L=-i*(H(i1,i1).*E(i2,i2)-Hc(i2,i2).*E(i1,i1));


% "feeding" terms
L=L+C1(i1,i1).*C1(i2,i2);
L=L+C2(i1,i1).*C2(i2,i2);
L=L+C3(i1,i1).*C3(i2,i2);
L=L+C4(i1,i1).*C4(i2,i2);
```

```
function rho=dndynfa(par,t,r0)

% Program to calculate the atomic dynamics of
% a trapped three level atom in interaction with two
% coherent light fields. The particle is oscillating
% in the trap at frequency ff with the velocity
% amplitude v.

% t in microseconds
% r0 ... initial condition

lam1 = 493;                    % Barium wavelengths
lam2 = 650;

O12   = par(1);                % Rabi frequencies
O23   = par(2);
D1    = par(3);                % detunings
D2    = par(4);
gl1   = par(5);                % linewidths
gl2   = par(6);
v     = par(7);                % velocity amplitude
ff    = par(8);                % trap frequency


L0  = b311(O12,O23,0 ,0 ,gl1,gl2);
dL1 = b311(O12,O23,1 ,0 ,gl1,gl2)-L0;
dL2 = b311(O12,O23,0 ,1 ,gl1,gl2)-L0;
DL  = 1000*v*(1/lam1*dL1+1/lam2*dL2);
L   = L0+D1*dL1+D2*dL2;

z=length(L0);
zh=sqrt(z);

% numerical integration
th=[0 t(length(t))];
[th,rhoh]=ode45('dndynfavec',th,r0,[],L,DL,ff);
rho=interp1(th,rhoh,t,'spline');
```

```
function rprime=dndynfavec(t,r,flag,L,DL,ff);

% function used in dndynfa.m
% calculates the derivative of the density matrix vector

rprime=(L+DL*cos(2*pi*t*ff))*r;
```

```
function L=b811(s1,s2,l1,l2,D1,D2,u,alpha)

% Program to calculate the Liouville operator
% for the Zeeman split eight-level system.

% S1, S2 ... saturation parameters
% L1, l2 ... laser linewidths
% D1, D2 ... detunings
% u       ... magnetic field
% alpha   ... angle between polarization and magnetic field

g1=15.1;        % Barium decay constants in MHz
g2=5.3;

O1=s1*g1;       % Rabi frequencies
O2=s2*g2;

gS=2;           % Lande factors
gP=2/3;
gD=4/5;

c=cos(alpha);
s=sin(alpha);
w3=3^0.5;



E=eye(8);
ii=(1:8)'*ones(1,8);
i1=reshape(ii',1,64);      % first index
i2=reshape(ii,1,64);    % second index



H=diag([D1,D1,0,0,D2,D2,D2,D2]+0.5*u*[-gS,gS,-gP,gP,-3*gD,-gD,gD,3*gD]);
HSP=-O1/w3*[ -c s ; s c ];
HDP=-O2/2/w3*[ w3*s 0 ; 2*c s ; -s 2*c ; 0 -w3*s ];

H(1:2,3:4)=HSP;   H(3:4,1:2)=HSP';
H(5:8,3:4)=HDP;   H(3:4,5:8)=HDP';

% Relaxation
C1=(2/3*g1)^0.5*E(:,1)*E(4,:);
C2=(2/3*g1)^0.5*E(:,2)*E(3,:);
```

```
C3=(1/3*g1)^0.5*(E(:,1)*E(3,:)-E(:,2)*E(4,:));
C4=(1/2*g2)^0.5*E(:,5)*E(3,:)+(1/6*g2)^0.5*E(:,6)*E(4,:);
C5=(1/6*g2)^0.5*E(:,7)*E(3,:)+(1/2*g2)^0.5*E(:,8)*E(4,:);
C6=(1/3*g2)^0.5*(E(:,6)*E(3,:)+E(:,7)*E(4,:));
C7=(2*l1)^0.5*(E(:,1)*E(1,:)+E(:,2)*E(2,:));
C8=(2*l2)^0.5*(E(:,5)*E(5,:)+E(:,6)*E(6,:)+E(:,7)*E(7,:)+E(:,8)*E(8,:));


CC=(C1'*C1+C2'*C2+C3'*C3+C4'*C4+C5'*C5+C6'*C6+C7'*C7+C8'*C8);


% effective Hamiltonian
H=H-i/2*CC;
Hc=H'.';


L=-i*(H(i1,i1).*E(i2,i2)-Hc(i2,i2).*E(i1,i1));


% feeding terms
L=L+C1(i1,i1).*C1(i2,i2);
L=L+C2(i1,i1).*C2(i2,i2);
L=L+C3(i1,i1).*C3(i2,i2);
L=L+C4(i1,i1).*C4(i2,i2);
L=L+C5(i1,i1).*C5(i2,i2);
L=L+C6(i1,i1).*C6(i2,i2);
L=L+C7(i1,i1).*C7(i2,i2);
L=L+C8(i1,i1).*C8(i2,i2);
```

```
function fl=rfb2(D2,par)

% Program to calculate excitation spectrum
% of a Barium ion used for fitting
% Laser at 650nm detuned (detuning D2 in MHz)

 D2null = par(1);                       % zero point of frequency axis
 sat1   = par(2);                       % saturations
 sat2   = par(3);
 l1     = par(4)/1000/2;                % laser linewidths in kHz
 l2     = l1;
 D1     = par(5);                       % detuning of the green laser
 u      = par(6);                       % magnetic field
 alpha  = par(7)/180*pi;                % angle between polarization
                                        %         and magnetic field
 faktor = par(8)*1000;
 offset = par(9);                       % dark counting rate

l=length(D2);
rs=zeros(64,l);
rhs=[1,zeros(1,63)]';

L0=b811(sat1,sat2,l1,l2,0,0,u,alpha);
dL1=b811(sat1,sat2,l1,l2,1,0,u,alpha)-L0;
dL2=b811(sat1,sat2,l1,l2,0,1,u,alpha)-L0;
L=L0+D1*dL1;

for n=1:l
    Ln=L+(D2(n)-D2null)*dL2;
    Ln(1,:)=zeros(1,64);
    Ln(1,1:9:64)=ones(1,8);
    rs(:,n)=Ln\rhs;
end
fl=faktor*real(sum(rs([19,28],:)))+offset;
```

```
function fl=anspecfa2(D2,par)

% Program to calculate excitation spectra used for fitting
% Red laser detuned
% The effect of the oscillation of the ion in the trap
% is considered using the matrix continued fraction formalism.

D2null = par(1);                 % zero point of frequency axis
S1     = par(2);                 % saturation
S2     = par(3);
D1     = par(4);                 % detuning of the green laser
l1     = par(5)/1000/2;          % linewidths in kHz
l2     = l1;
u      = par(6);                 % magnetic field
alpha  = par(7);                 % angle between polarization
                                 %         and magnetic field
v      = par(8);                 % velocity amplitude in m/s
ff     = par(9);                 % trap frequency
faktor = par(10);
offset = par(11);                % dark counting rate


lam1 = 493;
lam2 = 650;

% modulation index
modind = ceil(5*1000*v/lam1/ff);

L0    = b811(S1,S2,l1,l2 ,0, 0,u,alpha);        % Liouville matrix
dL1   = b811(S1,S2,l1,l2 ,1 ,0 ,u,alpha)-L0;
dL2   = b811(S1,S2,l1,l2 ,0 ,1 ,u,alpha)-L0;
DE    = 1000*v*(1/lam1*dL1+1/lam2*dL2);

z=length(L0);
zh=sqrt(z);

E=eye(z);

l=length(D2);

for m=1:l
   L=L0+D1*dL1+D2(m)*dL2;
```

```
    Sp=-0.5*(L+i*(modind+1)*ff*E)\DE;
    Sm=-0.5*(L-i*(modind+1)*ff*E)\DE;

    for n=modind:-1:1
        Sp=-0.5*(L+i*n*ff*E+0.5*DE*Sp)\DE;
        Sm=-0.5*(L-i*n*ff*E+0.5*DE*Sm)\DE;
    end;

    Ah=L+0.5*DE*(Sp+Sm);

    v=zeros(1,z);
    v(1,1:(zh+1):z)=ones(1,zh);
    A=[v;Ah];
    c=[1,zeros(1,z)]';
    r(:,m)=A\c;

end;

fl=faktor*real(sum(r([19,28],:)))+offset;
```

```
function g=k8n(t,par)

% Program to calculate the photon correlation
% (green-green) of a Barium ion

tnull  = par(1);            % zero point of the time axis
sat1   = par(2);            % saturation of the green
sat2   = par(3);            % and the red laser
l1     = par(4)/1000/2;     % laser linewidths in kHz
l2     = l1;
D1     = par(5);            % detuning of the green laser in MHz
D2     = par(6);            % detuning of the red laser in MHz
u      = par(7);            % magnetic field in MHz
alpha  = par(8)/180*pi;     % angle between polarization and
                            % magnetic field
faktor = par(9);
offset = par(10);


tr=(t-tnull)*2*pi/1000;
g=zeros(length(tr),1);


L=b811(sat1,sat2,l1,l2,D1,D2,u,alpha);

% steady state solution
Ln=L;
rhs=[1,zeros(1,63)]';
Ln(1,:)=zeros(1,64);
Ln(1,1:9:64)=ones(1,8);
ru=Ln\rhs;
norm=ru(19)+ru(28);


% initial condition
r0=zeros(64,1);
r0(1)  = ru(28)/norm;
r0(10) = ru(19)/norm;


% eigenvalues and vectors
[v,d]=eig(L);
d=diag(d);
f=v\r0;
```

```
% solution
for n=1:length(tr)
    rho=v*(exp(d*tr(n)).*f);
    g(n)=rho(19)+rho(28);
end;

g=real(g*faktor/norm)+offset;
```

8.4   Least-squares fit to data points

The fitting of theoretical curves to measured data points is a standard procedure that is outlined here:

Let y denote a physical quantity that is measured as a function of another physical quantity x. When x is set to a fixed value x_i, repeated mesurements of y_i allow one to determine the mean value and the variance σ_i^2. The dependence of y on x is described by a function f, whose specific form again depends on a set of parameters $p_1, \cdots, p_k$.

$$
\begin{aligned}
f : \mathbb{R} \times \mathbb{R}^k &\longrightarrow \mathbb{R} \\
(x, p_1, \cdots, p_k) &\longmapsto y = f(x, p_1, \cdots, p_k)
\end{aligned}
$$

The aim is to find the parameters $p_1^0, \cdots, p_k^0$ for which the function

$$
\begin{aligned}
\chi^2 : \mathbb{R}^k &\longrightarrow \mathbb{R} \\
(p_1, \cdots, p_k) &\longmapsto \sum_{i=1}^{N} \frac{(y_i - f(x_i, p_1, \cdots, p_k))^2}{\sigma_i^2}
\end{aligned}
$$

is minimal.

x may for example be the laser detuning and y the number of photomultiplier counts in a certain time delay. The photon counts obey a Poissonian distribution, i.e.

$$
\sigma_i^2 = y_i.
$$

There are several methods for searching the minimum of the χ^2 hypersurface. All fits in this paper are calculated with the function `leastsq.m` in the MATLAB toolbox. This function uses the Levenberg-Marquardt-algorithm, which combines the gradient search with the method of linearizing the fitting function [46]. Since for an arbitrary function f there is in general more than one minimum, the search result depends on the initial condition.

The result of the fit can be tested by calculating the reduced chi-square χ_ν^2 defined as:

$$
\chi_\nu^2 = \frac{1}{N - k} \chi^2
$$

The factor N-k is the number of degrees of freedom left after fitting N data points to the k parameters. When $\chi_\nu^2 \approx 1$ the fit is good, i.e. the deviations correspond to what is expected by statistical fluctuations. Large or very small values generally indicate that the data cannot be appropriately described by the fitting function or that the variances σ_i^2 differ from the expected ones.

8 Appendix

The uncertainties on the fit parameters can be estimated by calculating the second derivative of χ^2_ν at the minimum or equivalently the curvature of the corresponding parabola. The uncertainties are defined by the following equation

$$\chi^2_\nu(p_i^0 \pm \Delta p_i) = \chi^2_\nu + 1$$

which yields

$$\Delta p_i = \frac{1}{\sqrt{\frac{1}{2} \frac{\partial^2 \chi^2_\nu}{\partial p_i^2}}}$$

As an example for the determination of the uncertainties we chose the fit to the measured excitation spectrum plotted in figure 6.1. χ^2_ν is calculated as a function of the parameter p_i in a small region $\mathcal{P}_i = [p_i^0 - \Delta p_i, p_i^0 + \Delta p_i]$ around the minimum p_i^0 while the other parameters are kept fixed:

$$\left(\chi^2_\nu\right)_i : \mathcal{P}_i \longrightarrow \mathbb{R}$$

$$p_i \longmapsto \chi^2_\nu(p_1^0, \dots, p_i, \dots, p_k^0) \approx \chi^2_\nu(p_1^0, \dots, p_k^0) + \frac{1}{2} \frac{\partial^2 \chi^2_\nu}{\partial p_i^2} \left(p_i - p_i^0\right)^2$$

Figure 8.1 shows a calculation of these functions using the fit to the excitation spectrum plotted in figure 6.1. The dots are the calculated values of χ^2_ν and the solid lines are the fitted parabolas. With the exception of the dependence on the angle α the parabolic shape of χ^2_ν around the minimum is clearly visible. The curvatures of these parabolas are a good approximation of the second derivatives around the minimum.

The zero point of the frequency axis Δ_{g0} depends on the drift of the reference resonator relative to the Barium resonances.
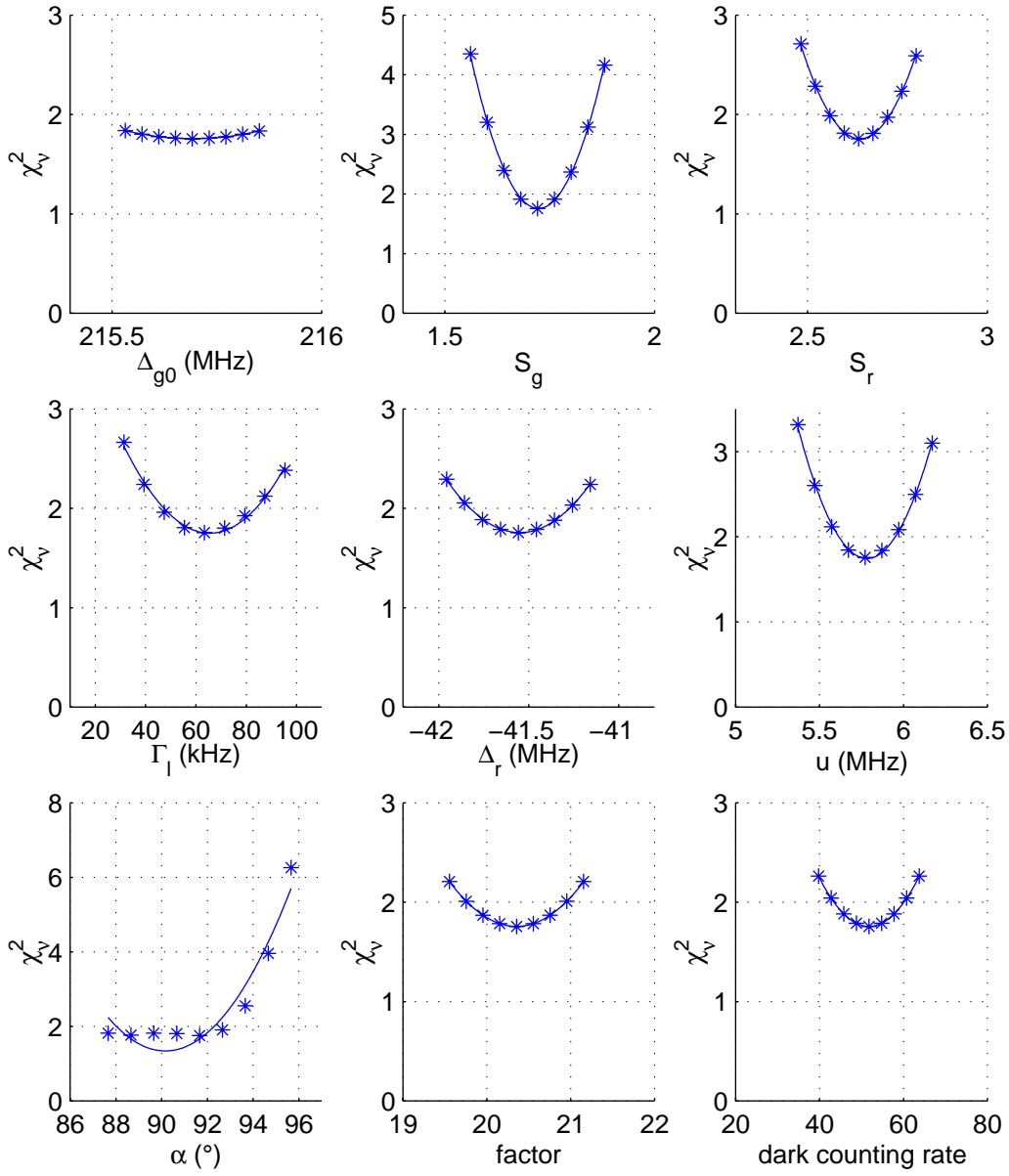
Figure 8.1: Calculation of the uncertainties of the parameters using the fit in figure 6.1. Parameters: Zero point of the frequency axis Δ_{g0}=215.7 MHz, S_g = 1.7 ± 0.1, S_r = 2.6 ± 0.2, Γ_l = 60 ± 40 kHz, Δ_r = −41.4 ± 0.5 MHz, u = 5.8 ± 0.3 MHz, α = 91 ± 5°, factor=20±1, dark counting rate 50±20. Reduced chi-square χ^2_ν=1.6.

8.5 Excitation spectra of Calcium ions

In two other experimental projects performed in our research group ^{40}Ca$^+$ ions are used for quantum optical experiments [47–49]. The fine structure level scheme of Ca$^+$ is the same as for Ba$^+$ ions, however, with different transition wavelenghts and decay constants. Figure 8.2 shows the relevant part of the fine structure level scheme of Ca$^+$ with the transition wavelengths indicated. The S $\Leftrightarrow$ P and the P $\Leftrightarrow$ D transitions are dipole-allowed whereas the D levels are metastable with a lifetime of 1s.
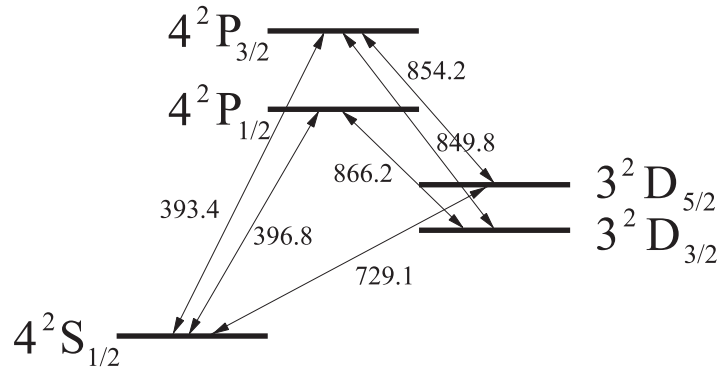
Figure 8.2: Fine structure level scheme of ^{40}Ca$^+$. All wavelengths are given in nm [20].

When the ion is illuminated by two coherent light fields at 397 nm and 866 nm, which corresponds to the $4^2S_{1/2} \Leftrightarrow 4^2P_{1/2}$ and $4^2P_{1/2} \Leftrightarrow 3^2D_{3/2}$ transitions, and a homogenous magnetic field is applied then the fluorescent light emitted by the ion can be perfectly described by the model introduced in chapter 2 and 3. In this model the atomic system is completely characterized by its decay constants. The decay constants of Ca$^+$ are: $\Gamma_{SP}^{Ca} = 21.58$ MHz and $\Gamma_{PD}^{Ca} = 1.35$ MHz.

Figure 8.3 shows an excitation spectrum of Ca$^+$. The ion is optically cooled on the $4^2S_{1/2} \Leftrightarrow 4^2P_{1/2}$ transition with the laser at 397 nm while the laser at 866 nm is tuned over the Ca$^+$ resonance. The solid line is a fit to the data that has been calculated using the MATLAB program `rfb2.m` (see appendix 8.3). In the subprogram `b811.m` the Ba$^+$ decay constants have been replaced by those of Ca$^+$. The spectral shape is different for Barium and Calcium ions owing to the different branching ration Γ_{SP}/Γ_{PD}.

By inserting the Calcium constants into equation (3.54) we obtain the following relation
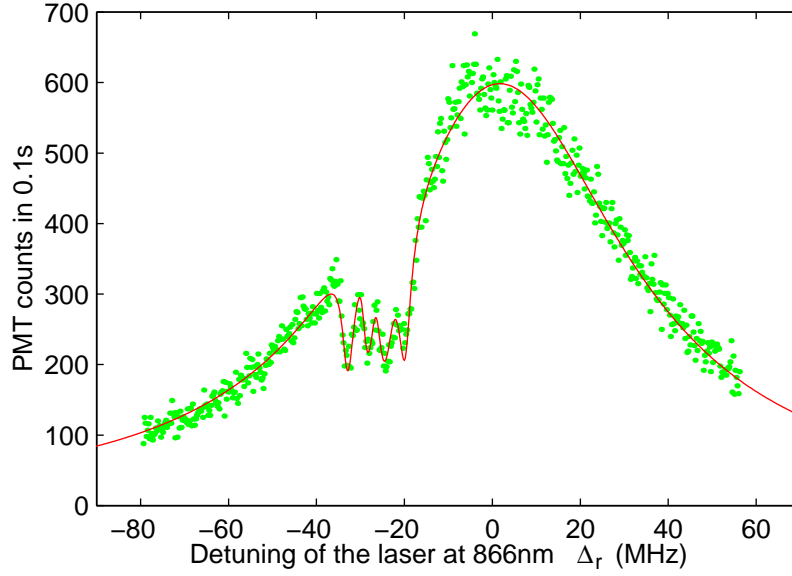
Figure 8.3: Excitation spectrum of Ca$^+$. Parameters: S_g=0.54±0.03, S_r=3.9±0.3, Δ_g=-26±1 MHz, u=2.9±0.6 MHz, α=100±10°, Γ_l=300±300 kHz.

between the saturation parameters and the laser intensities:

$$I_{397}(S_g) = 361 \cdot S_g^2 \, \frac{mW}{cm^2}$$

$$I_{866}(S_r) = 2.17 \cdot S_r^2 \, \frac{mW}{cm^2}$$

Please note that the calculations are made with the assumption that the magnetic field is perpendicular to the propagation direction of the lasers and that the ion is observed in the direction of the magnetic field.

Bibliography

[1] R. H. BROWN and R.Q.TWISS, Nature **177**, 27 (1956)

[2] R. H. BROWN and R.Q.TWISS, Proc.R.Soc.A **242**, 300 (1957)

[3] D. STOLER, Phys.Rev.Lett. **33**, 1397 (1974)

[4] H. CARMICHAEL and D. WALLS, J.Phys. **B9** (9), 1199 (1976)

[5] H. KIMBLE, M. DAGENAIS, and L. MANDEL, Phys.Rev.Lett. **39**, 691 (1977)

[6] M. DAGENAIS and L. MANDEL, Phys.Rev. **A18**, 2217 (1978)

[7] D. WALLS, Nature **306**, 141 (1983)

[8] P. ZOLLER and D. WALLS, Phys.Rev.Lett. **47**, 709 (1981)

[9] W. VOGEL and R. BLATT, Phys.Rev. **A45** (5), 3319–3328 (1992)

[10] J. RARITY and P. TAPSTER, Phys.Rev.Lett. **64**, 2495 (1990)

[11] W. LAMB and R. RETHERFORD, Phys.Rev. **72**, 241 (1947)

[12] H. BETHE, Phys.Rev. **72**, 339 (1947)

[13] V. WEISSKOPF and E.WIGNER, Z.Phys. **63**, 54 (1930)

[14] L. HILICO, D. TOUAHRI, F. NEZ, and A. CLAIRON, Rev.Sci.Instrum. **65** (12) (1994)

[15] W. DEMTRÖDER, *Laserspektroskopie*, Springer-Verlag (1993)

[16] H. DEHMELT and P. TOSCHEK, Bull.Am.Phys.Soc. **20**, 61 (1975)

[17] D. WINELAND and H. DEHMELT, Bull.Am.Phys.Soc. **20**, 637 (1975)

[18] W. NEUHAUSER, G. FÖRSTER, P. TOSCHEK, and H. DEHMELT, Phys.Rev. **A22**, 1137 (1980)

Bibliography

[19] A. GALLAGHER, Phys.Rev. **157**, 24 (1967)

[20] D. JAMES, Appl.Phys. **B66**, 181–190 (1998)

[21] R. LOUDON, *The quantum theory of light*, Oxford science publications, second edition (1983)

[22] T. MAYER-KUCKUK, *Atomphysik*, Teubner (1994)

[23] A. LINDNER, *Grundkurs Theoretische Physik*, Teubner (1994)

[24] C. COHEN-TANNOUDJI, in *Frontiers in Laser Spectroscopy, Les Houches 1975, session XXVII*, edited by Balian, Haroche, and Liberman, North Holland, Amsterdam (1977)

[25] M. SCHUBERT, *Intensitätskorrelationen in der Resonanzfluoreszenz eines einzelnen gespeicherten Ions*, Dissertation, Universität Hamburg (1991)

[26] I. SIEMERS, *Über die Dunkelresonanz im Anregungsspektrum eines einzelnen Ions*, Dissertation, Universität Hamburg (1991)

[27] C. COHEN-TANNOUDJI, B. DIU, and F. LALOË, *Quantenmechanik 2*, Walter de Gruyter, Berlin, New York (1997)

[28] W. PAUL, O. OSBERGHAUS, and E. FISCHER, *Forschungsberichte des Wirtschafts-und Verkehrsministeriums Nordrhein-Westfalen*, number 415 (1958)

[29] R. GOSH, *Ion traps*, Clarendon Press, Oxford (1995)

[30] G. HORVATH, R. THOMPSON, and P. KNIGHT, Contemporary Physics **38** (1), 25–48 (1997)

[31] D. REISS, *Laserkühlung eines gespeicherten Ions*, Diplomarbeit, Universität Hamburg (1995)

[32] D. REISS, A. LINDNER, and R. BLATT, Phys.Rev. **A54** (6), 5133–5140 (1996)

[33] F. DIEDRICH, J. BERQUIST, W. ITANO, and D. WINELAND, Phys.Rev.Lett. **62**, 403 (1989)

[34] C. RAAB, *Ein Laserspektrometer zur Untersuchung gespeicherter Ba^+-Ionen*, Diplomarbeit, Universität Göttingen (1996)

[35] H. LANGFISCHER, *Frequenzstabilisierung eines Diodenlasers bei 650 nm zur Spektroskopie an einzelnen Barium-Ionen*, Diplomarbeit, Universität Innsbruck (1998)

[36] C. RAAB, J. BOLLE, H. OBERST, J. ESCHNER, F. SCHMIDT-KALER, and R. BLATT, Appl.Phys. **B67** (6), 683–688 (1998)

[37] J. BOLLE, *Spektroskopie und nichtklassische Fluoreszenzeigenschaften von einzelnen gespeicherten Ba^+-Ionen*, Dissertation, Universität Innsbruck (1998)

[38] M. LITTMAN and H. METCALF, Appl.Opt. **17**, 2224 (1978)

[39] R. POUND, Rev. Sci.Instr. **17**, 490 (1946)

[40] G. THALHAMMER, *Frequenzstabilisierung von Diodenlasern bei 850, 854 und 866 nm mit Linienbreiten im Kilohertz-Bereich*, Diplomarbeit, Universität Innsbruck (1999)

[41] T. SAUTER, W. NEUHAUSER, R. BLATT, and P. TOSCHEK, Phys.Rev.Lett. **57**, 1696–1698 (1986)

[42] J. BERGQUIST, R. HULET, W. ITANO, and D. WINELAND, Phys.Rev.Lett. **57**, 1699–1702 (1986)

[43] I. SIEMERS, M. SCHUBERT, R. BLATT, W. NEUHAUSER, and P. TOSCHEK, Europhys.Lett. **18** (2), 139–144 (1992)

[44] M. SCHUBERT, I. SIEMERS, R. BLATT, W. NEUHAUSER, and P. TOSCHEK, Phys.Rev. **A52** (4), 2994 (1995)

[45] J. CIRAC, R. BLATT, A. PARKINS, and P. ZOLLER, Phys. Rev. **A48**, 2169 (1993)

[46] P. BEVINGTON, *Data Reduction and Error Analysis for the Physical Science*, McGraw-Hill Book Company (1969)

[47] H.-C. NÄGERL, *Ion Strings for Quantum Computation*, Dissertation, Universität Innsbruck (1998)

[48] H.-C. NÄGERL, D. LEIBFRIED, F. SCHMIDT-KALER, J. ESCHNER, and R. BLATT, Opt. Express **3**, 89 (1998)

[49] H.-C. NÄGERL, W. BECHTER, J. ESCHNER, F. SCHMIDT-KALER, and R. BLATT, Appl. Phys. **B66**, 603 (1998)

Danksagung

Ich bedanke mich

- bei Herrn Prof. Rainer Blatt für die Möglichkeit, diese Arbeit in seiner Arbeitsgruppe anzufertigen, und für die interessante Themenstellung. Durch seine Führung hatte ich die Möglichkeit, in die spannende Welt der Wissenschaft einzudringen und an ihr teilzuhaben.

- bei allen Mitgliedern der Arbeitsgruppe für ihre freundliche Aufnahme. Sie alle haben mir immer mit Rat und Tat beiseite gestanden.

- bei Dipl.-Phys. Christoph Raab für die Geduld, mit der er mir die Einzelheiten des experimentellen Aufbaus erklärt und alle meine Fragen beantwortet hat, und für die Hilfsbereitschaft und tatkräftige Unterstützung während der letzten eineinhalb Jahre.

- bei Dr. Jürgen Eschner für seine Unterstützung und zahlreiche Diskussionen. Von ihm habe ich viel über die physikalischen Modelle und deren Implementierung in Computerprogrammen gelernt.

- bei Dr. Joachim Bolle für die kameradschaftliche Zusammenarbeit im Labor und bei Mag. Helmut Langfischer dafür, daß er mich zu Beginn meiner Arbeit mit dem roten Laser vertraut gemacht hat.

- bei meinem Freund Gregor Thalhammer: Er stand mir mit seinem Wissen und seiner Geschicklichkeit oft beiseite. In Zusammenarbeit mit ihm konnte die Effizienz und Rechengeschwindigkeit vieler Computerprogramme erheblich gesteigert werden.

- bei Jürgen Eschner, Christoph Raab und David Stevens von der University of Oxford für die Durchsicht von Teilen vorläufiger Stadien dieser Arbeit.